TWO-FLUID SIMULATION OF AN AIRLIFT LOOP REACTOR WITH FLUENT

Jeannet Pols

Master's thesis

Delft University of Technology
Department of Applied Physics

Delft, October 2001

Kramers Laboratorium voor
Fysische Technologie
Prins Bernhardlaan 6
2628 BW Delft

Professor: prof. dr. ir. H.E.A. van den Akker
Supervisors: dr. R.F. Mudde

Abstract

Airlift loop reactors are frequently applied in the chemical and biological industry. They are made of two sections interconnected at the top and bottom, with an ungassed downcomer and a gassed riser. In this type of reactor the density-difference between the sections supplies the needed driving force needed for the liquid circulation. Numerical simulations are recognised as a primary tool for improving the performance of process equipment for scaling up of the airlift loop reactors.
Three dimensional simulations of two phase (gas and liquid) bubbly flow in a rectangular airlift loop reactor with two downcomer sections have been obtained using the CFD package Fluent 4.5.6. The simulations are based on a full two fluid model with a modified $k - \epsilon$ model for the turbulence. As the interfacial forces between the two phases, the drag force and virtual mass have been taken into account.
The results are compared with an one-dimensional mechanical energy balance and are found to be in good agreement when a 'false' time step of $1 \cdot 10^{-2} s$ is used. The mean riser and downcomer gas fractions are too high in the simulations with time step of $1 \cdot 10^{-3} s$, in comparison with this one-dimensional balance. Probably this is caused by the virtual mass.
The interface turbulent momentum transfer terms (the turbulent diffusion terms), which can only be calculated for a dilute secondary phase are necessary for realistic results. Outlets with a gas disengagement zone at the top can not be calculated well due to this limitation. An outlet type with fixed velocities on top has to be chosen, which works well but misses the flexibility for the gas throughput and velocities.
After refining the grid the flow field changes and gives better results, but the calculation time increases. The minimal grid size has to be 30 x 10 x 80 (width x depth x height). Furthermore, two symmetry axis can used namely, one vertical plane through the riser and one vertical between the front and back wall through the riser and downcomer. With the use of both symmetry axis the calculation time is reduced significantly.

Samenvatting

In the chemische en biologische industrie wordt steeds meer gebruik gemaakt van de airlift loop reactor. De airlift loop reactor bestaat uit twee secties, een downcomer en een riser met een gas inlaat onder in de riser. Beide secties zijn aan de bodem en de top van de reactor met elkaar verbonden. Het dichtheid verschil tussend de beide secties is de drijvende kracht voor de circulatie van de vloeistof. Om een beeld te krijgen van de hydrodynamica in verschillende airlift loop reactors voor bijvoorbeeld opschalling is numerieke simulatie belangrijk.
In het CFD programma Fluent 4.5.6. is een drie dimensionaal rechthoekige airlift loop reactor met twee fase stroming (gas en vloeistof fase) gesimuleerd. Deze simulaties zijn gebaseerd op een twee fase model, Euler-Euler model, en voor de turbulentie is gebruik gemaakt van het $k - \epsilon$ model. Verder zijn de drag force en virtuale masss meegenomen als de krachten tussen de gas en vloeistof fase.
Gas fractie en gas en vloeistof snelheden uit simulaties met een tijdstap van $1 \cdot 10^{-2} s$ komen goed overeen met de waarden die zijn gevonden met een 1 dimensionale mechanische energie balans. Bij simulaties met een kleinere tijdstap, $1 \cdot 10^{-3} s$, zijn de gas fractie in de downcomer veel hoger in vergelijk met waarden uit deze mechanische energie balans. De waarschijnlijke oorzaak hiervan is de berekening van de virtuale massa in Fluent.
Om goede resultaten te kunnen krijgen is het belangrijk dat de turbulente diffusie termen (interphase turbulent momentum transfer terms) worden meegenomen. Als deze termen aan staan is het alleen mogelijk om berekeningen te doen aan reactors met een redelijke vloeistof fase. Berekeningen met aan de top een volume met vrijwel alleen gas is dus niet mogelijk. De uitlaat van de airlift reactor moet dus op een andere manier worden nageboots dit wordt gedaan met behulp van vastaande gas en vloeistof snelheden net onder de uitlaat. Dit werkt redelijk goed, maar een flexibele gas doorlaat wordt in dit geval gemist.
Simulaties met meer grid cellen, fijner grid, geven betere resultaten. Het nadeel hiervan is dat de tijd van berekening behoorlijk toe neemt. Om dit te compenseren kan gebruik worden gemaakt van twee symmetrie assen, een vertikaal door de riser en de ander vertikaal tussen de voor- en achterwand van de airlift door de riser en downcomer.

List of symbols

Roman Symbols

Symbol	Description	S.I. units
A	Surface	m^2
b	Turbulence quantity for disperse phase	-
C_D	Drag coefficient	-
C_l	Constant of Magnes force	-
C_{vm}	Virtual mass coefficient	-
C_w	Exchange coefficient	$kgm^{-3}s^{-1}$
C_β	Dispersed phase turbulence parameter	-
C_μ	$k-\epsilon$ model parameter	-
C_0	Distribution parameter of the drift-flux model	-
C_1	Parameter of the drift-flux model	-
$C_{1\epsilon}$	$k-\epsilon$ model parameter	-
$C_{2\epsilon}$	$k-\epsilon$ model parameter	-
d_2	Bubble diameter	m
D_{12}^t	Binary diffusion tensor	m^2s^{-1}
E	Emperical constant	-
F	Force	$kgm^{-2}s^{-2}$
F_w	Interaction force	$kgm^{-2}s^{-2}$
g	Gravity acceleration	$m^{-1}s^{-2}$
G_b	Rate of Production of turbulent kinetic energy due to thermal buoyancy	$kgm^{-1}s^{-3}$
G_k	Rate of production of turbulent kinetic energy due to velocity gradients	$kgms^{-3}$
H	Riser or Downcomer length	m
I	Unity tensor	-
k	Turbulent kinetic energy	m^2s^{-2}
K_f	Overal friction loss coefficient	-
K_{21}	Interface momentum exchange coefficient	$kgm^{-3}s^{-1}$
L	Macroscopic lenth scale	m
n	Normal vector component	m
n	Richardson & Zaki-exponent	-

N_t	Total number of cells	-
P	Pressure	$kgm^{-3}s^{-1}$
$\overrightarrow{\overrightarrow{S}}$	Mean strain rate tensor	s^{-1}
t	Time	s
T	Time interval	s
U	Mean velocity component	ms^{-1}
$U^{'}$	Fluctuating part of the velocity component	ms^{-1}
u^*	Law of the wall velocity	ms−1
U_d	Drifting velocity vector	ms^{-1}
U_r	Local mean velocity vector	ms^{-1}
V	Volume	m^3
v_{21}	Slip velocity	ms^{-1}
v_{inf}	Slip velocity of a single bubble	ms^{-1}
y	Distance	m

Greek Symbols

Symbol	**Description**	**S.I. units**
α	Gas volume fraction	-
Γ	Flow property	
Δn_p	distance from point p to the wall	m
ϵ	Turbulent energy dissipation	m^2s^{-3}
η_r	Two phase turbulence timescale ratio	-
κ	Karman's constant	-
λ	Kolmogorov lenght scale	m
μ	Dynamic viscosity	$kgm^{-1}s^{-1}$
ρ	Density	kgm^{-3}
ν	Kinematic viscosity	m^2s^{-1}
ξ	Two-phase turbulence timescale ratio	-
Π_k	Two phase flow turbulence source term	m^2s^{-3}
Π_ϵ	Two phase flow turbulence source term	m^2s^{-4}
τ_{mol}	moluculair stress tensor	$kgm^{-1}s^{-2}$
τ_{Re}	Reynolds stress tensor	$kgm^{-1}s^{-2}$
τ_w	Shear stress	$kg.m^{-1}s^{-2}$
τ_1^t	Turbulent characteristic time of continues phase	s
τ_{12}^t	Turbulent characteristic time of continues phase viewed by particle	s
τ_{21}^F	Mean particle relaxation time	s
ϕ	Mass flow rate	kgm^{-3}
σ_{21}	Turbulent Schmidth number	-

Subscripts

Symbol	Description
bubble	Based on a bubble diameter
C	Central cell centre value
d	Downcomer
D	Downstream cell centre value
D	Drag
eff	Effective
f	Face value
gas	Secondary phase (gas phase)
i	Cartesian co-ordinates
k	Phase
l	Lift
liq	Primairy phase (liquid phase)
p	Point p near the wall
r	Riser
sup	superficial
t	Turbulence
U	Upstream cell centre value
vm	Virtual mass
x	Width
y	Depth
z	Height

Superscript

Symbol	Description
t	Turbulence
$'$	Fluctuation
$*$	Point in log-law layer

Contents

Chapter 1

Introduction

Bubbly reactors are more and more applied in the chemical industry, biochemical fermentation and biological wastewater treatment processes. In these processes a good contacting between a gas and liquid phase is necessary. Among the various reactor types used, the airlift loop reactor is found. The airlift loop reactor is made of two sections interconnected at top and bottom. One section (riser) is gassed, while the other (downcomer) is not. The liquids starts to circulate as a consequence of the density difference between the bubble mixture in the riser and the liquid in the downcomer. The airlift can handle large quantities of liquid and gas on a continuous basis with limited shear and is therefore popular as a gas liquid contactor.

Optimisation of an airlift loop reactor can provide large financial benefits due to larger process capacities. This has led to increased interest in modeling the airlift loop reactor and other multiphase flow reactors. However, reliable multiphase reactor models that can be used with confidence for improving existing processes and scale up are not available yet. Numerical simulation is being recognised as a primary tool for improving the performance of process equipment. In particular, a reliable fluid dynamic reactor model is a great benefit for scale-up of chemical reactors. Dynamic numerical simulation is thus on the agenda of most big chemical companies and many scientific research laboratories.

For design operation and control purposes an accurate simulation of the reactor performance is essential. The model must include mass transfer, flow configuration and hydrodynamics. However, modeling of an airlift loop reactor is still difficult because the hydrodynamics of the flow (particularly the coalescing behaviour of organic liquid mixtures generally encountered in industry) is not completely understood. A simple one dimensional model based on balance equations in order to predict hydrodynamic parameters: the gas hold-up and the liquid circulation velocity, can used. However, it does rely on empirical input, like friction factors and axial dispersion coefficient and the details of the flow at the top and bottom of the column can not be completely resolved. A greater degree of detail of these flows can be obtained via Computational Fluid Dynamics (CFD).

1.1 Project

The goal of this thesis is to simulate an airlift loop reactor using the CFD Package Fluent. Fluent is a common tool at the Kramers Laboratory of the University of Technology of Delft. The main question is: Can the airlift loop reactor be simulated with the help of the package Fluent in the right way? This question can be divide in the following questions:

- Which parameters, forces are necessary to simulated an airlift loop reactor;
- What are the restrictions to simulate an airlift loop reactor with Fluent.

These questions will be addressed in this project with the approach which is shown in figure 1.1. In the first place the airlift loop reactor has to be simulated in a right

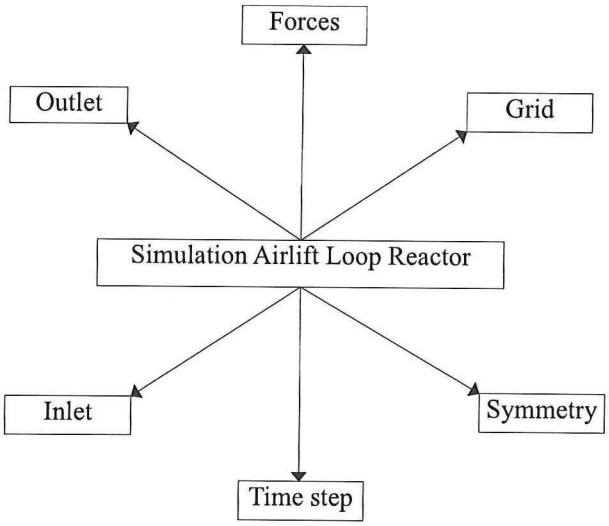

Figure 1.1: Approach of this project

way. After this simulation there is a look for the parameters which are really necessary and which can be neglected. Therefore, simulations are done with different outlet, time steps, gas inlet fraction, inlet geometry, forces, symmetries and grid size.
In section 2 the airlift loop reactor is described in detail, with advantages and disadvantages of the airlift reactor. Furthermore an one-dimensional model based on an energy balance is given. In chapter 3 the theory applied in this project is combined, the first part describes the two-phase flow, followed by the turbulence model and the numerical solver Fluent. The cases are described and the resulting discussed in chapter 4 and 5 ending in chapter 6 with the conclusions and recommendation.

Chapter 2

Airlift Loop Reactor

Airlift Loop Reactors (ALR) are pneumatic reactors and are different from the other commonly used pneumatic reactor, the bubble column. The ALRs are comprised of four distinct zones, each with its own distinct flow pattern, which divide the reactor into separate upward and downward (two-phase) flow regions. The zones enable macroscale liquid circulation around the loop. The first zone, in which the gas is sparged is called the 'riser'. This section has the higher gas hold-up. Furthermore, most of the gas-liquid mass transport takes place here. The liquid leaving the top of the riser enters a gas disengagement zone, where depending on its specific design some or most of the dispersed gas is removed. The gas-free liquid (or a dispersion of lesser hold-up) flows in the 'downcomer', the third zone. Then it travels to the bottom of the device, the fourth zone and after that it re-enters the riser. Thus, the liquid phase circulates continuously around the loop.
The liquid circulation is caused by the difference in the gas hold-up that exists between the riser and the downcomer. In turn, this creates a hydrostatic pressure difference between the bottom of the riser and the bottom of the downcomer, which acts as the driving force for the liquid circulation. The airlift, which is simulated in this thesis is described section 2.4.

2.1 Different types of Airlift Loop Reactor

ALRs are commonly divided into two types based on their physical structure: the internal-loop and external-loop ALRs. Internal-loop ALRs are baffled vessels where baffles are placed within a bubble column to provide the distinct flow channels of the loop. Concentric tube and split vessel ALRs are examples of internal-loop ALRs. External-loop ALRs are constructed of separate conduits which are attached at the top and bottom by horizontal conduits to form the circulation loop.

The modeling and scale up of ALRs is complicated by the interaction of the principle parameters, gas hold-up and liquid velocity, and consequently mass transfer

and mixing intensity. At any specific gas flow rate there will be a given difference in gas hold-up between the riser and downcomer ($\Delta\alpha_{gas} = \alpha_{gas,r} - \alpha_{gas,d}$) which will dictate the liquid circulation velocity around the loop. In order to change the mass transfer or mixing in the ALR, the incoming gas flow rate must be changed resulting in a new $\Delta\alpha_{gas}$ and liquid circulation velocity. All the geometric factors which influence the pressure drop around the loop, such as reactor height, ratio of downcomer/riser cross-sectional areas, gas-liquid separator configuration, influence the ALR operation. Therefore, in spite of the many design correlations in literature for liquid circulation velocity, gas hold-up, mixing and mass transfer, there are as yet no general correlations which are applicable to all ALRs.

2.2 Advantages of the airlift loop reactor

Pneumatics reactors, such as ALRs and bubble columns offer several advantages over stirred tank reactors (STR) [Siegel and Robinson, 1992]. Their simple construction is a primary advantage. Since there are no moving mechanical parts needed for agitation, there is a reduced danger of contamination through seals or magnetically-driven agitators. The vertical orientation of these reactors, as well as the lack of internals, facilitate easier cleaning and sterilization. The injected gas serves the dual function of aeration and agitation. This promotes efficiency in the overall energy balance, eliminating the need for separate expenditure of energy for agitation.

When compared with bubble columns, ALRs have the additional advantages of loop reactors, such as increased heat and mass transfer capacity enhanced plug flow behaviour and a reduction of the energy consumption for mixing.

Another advantage of ALRs over bubble columns and STRs is related to the shear stress imposed by the turbulent field in the medium. In the ALR the field of shear is relatively constant throughout the reactor. The fluid motion is induced by differences in the mean densities between the riser and downcomer sections of the reactor. Therefore, there is an overall directionality of liquid flow. In contrast, in bubble columns and STRs the energy source inducing fluid motion is local. The shear forces in bubble columns will be greatest adjacent to the gas sparger and dissipate with distance from the sparger. In STRs, a region of very high shear exists near the agitator, which decreases with increasing distance from the agitator.

In ALRs the fluidisation of solids is not a direct consequence of the bubbling of gas, but rather due to the liquid circulation within the reactor. Therefore, these reactors offer the possibility of very simple and highly effective solids fluidisation. This indicates a high potential for application in three-phase processes where gas, liquid and solids must be brought into contact. Thus, the ALR is an attractive option for slurry reactors.

2.3 Disadvantages of the airlift loop reactor

It seems to be very difficult to establish an economically optimal condition for operation performance of airlift loop reactors, since the theoretical model to predict the flow characteristics has not been exactly built up yet. It may be commonly accepted that one of the main factors, which make it extremely difficult, is the transitions of the flow pattern of the gas-phase. When gas-liquid mixtures flow upward in a vertical pipe, the two phases can distribute in a number of patterns, each characterizing the radial and/or axial distribution of liquid and gas. The flow is usually quite chaotic, and the phase distributions are difficult to describe. In figure 2.1 different

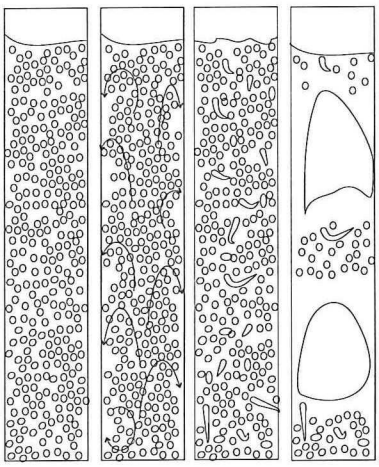

Figure 2.1: Different flow regime at different gas fractions with left the lowest gas fraction and right the highest gas fraction (a) Homogeneous bubble flow (b) Turbulent bubble flow (c) Churn flow (d) Slug or plug flow

flow regimes are shown. At a given liquid volume, different superficial gas velocities result in different flow modes.

2.4 Geometry

The airlift loop reactor, which is simulated, is rectangular with a central riser and two downcomers channels, one at each side of the riser, see figure 2.2. Water and air are taken for the two phases. The riser and downcomer are 10 and 13 cm in width, respectively and the depth of the column is 12 cm. The total height of the column is 120 cm, with a free surface around 105 cm of the total height of the column. The internal wall starts at a height of 15 cm above the bottom and ends at 90 cm of the total column height. The sparger is located in the bottom part of the riser. It is a

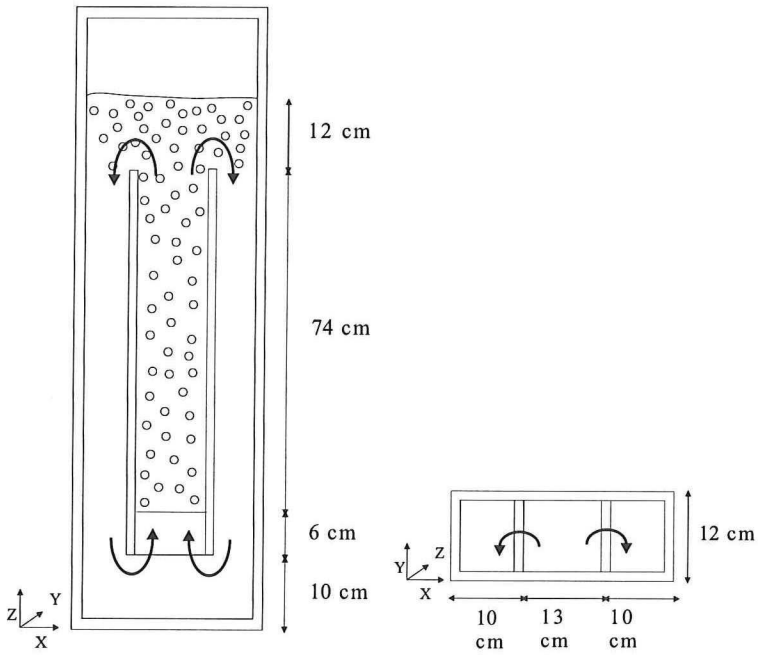

(a) side view (b) top view

Figure 2.2: Airlift loop reactor (a) side view of the airlift loop reactor (b) top view of the airlift loop reactor

rectangular box with the same cross-sectional area as the riser and a height of 7.5 cm. There are different rectangular flow channels in this part of the riser, depending on the gas inlet geometry, which will be described in section 4.2.2. The flow channels give more friction in this part of the airlift. The gas enters the riser through the inlet that forms the top lid of the box sparger at 22.5 cm above the bottom of the airlift. The air is introduced in the form of spherical bubbles with a diameter of 3 mm. In most simulations only one quarter of the reactor is simulated: the vertical plane through the middle of the riser as well as the vertical plane between the front and back wall through the riser and both downcomers are assumed to be planes of symmetry. In the other simulations only the first symmetry axis is present, so one half of the airlift is simulated.

2.5 Airlift modeling

The hydrodynamics of airlift loop reactors can be treated on the basis of a simple one-dimensional mechanical energy balance that calculates the liquid circulation by balancing the energy input via the gas flow to the dissipation due to friction. Mass and heat balance as well as chemical reactions are added to the hydrodynamical equations. However, the modeling does rely on empirical input, like friction factors and axial dispersion coefficients. These vary from airlift to airlift. More importantly the details of the flow at the top and bottom of the riser and downcomer can not be completely resolved. A greater degree of detail of these flows can be obtained via CFD.

The simple one-dimensional mathematical model is based on general balance equations for gas-liquid systems. The airlift loop reactor (see section 2.4) is divided into four parts, namely the riser and downcomer, the top (part above the internal baffle) and bottom (part below the internal baffle). In each part of the reactor, the flow is assumed steady-state and fully developed.

2.5.1 Mechanical energy balance

The density of both phases is assumed to be constant in the airlift loop reactor. The volume flow rates are written as [Couvert et al., 2000]:

$$\phi_{k,r} = A_r U_{k,r}^{sup} \alpha_{k,r} \tag{2.1}$$

$$\phi_{k,d} = A_d U_{k,d}^{sup} \alpha_{k,d} \tag{2.2}$$

where k=liq denotes the liquid phase, k=gas the gas phase, r and d denotes the riser and downcomer, respectively. ϕ is the volume flow rate, A the surface of the cross-section of the riser and downcomer, U the superficial velocity of the gas/liquid and $\alpha_{k,r}$ and $\alpha_{k,d}$ are the gas and liquid fraction in the riser and downcomer, respectively.

The one dimensional model for the flow is assuming: steady-state, uniform gas fraction in the riser, α_r and zero gas fraction in the downcomer, $\alpha_d = 0$. In a steady state, the hydrostatic pressure difference between riser and downcomer (ΔP) is the driving force for liquid circulation:

$$\Delta P = (\alpha_r - \alpha_d)\Delta\rho g H \tag{2.3}$$

where α is the average gas hold-up, $\Delta\rho$ is the density difference between the liquid and the gas phase and H the riser and downcomer length. The pressure drop due to overall friction losses along the circulation loop is expressed as

$$\Delta P = K_f \frac{1}{2}\rho_{liq}(U_{liq}^{sup})^2 \tag{2.4}$$

where K_f is the overall friction loss coefficient and U_{liq}^{sup} the superficial liquid velocity in the riser. The friction loss factors are estimated using standard relations for wall friction. The friction is dominated by the expansion after the flow channels through the sparger and by the flow reversal at both entrance and exit of the riser in the airlift. For the airlift, which is used an estimation relative to the superficial riser gas velocity of $K_f = 4.3$ is found, see appendix A.
Combination of equation 2.3 and 2.4 leads to a stationary hydrodynamic force balance

$$(\alpha_r - \alpha_d)\Delta\rho g H = K_f \frac{1}{2}\rho_{liq}(U_{liq}^{sup})^2 \tag{2.5}$$

Coupling between the gas hold-up and superficial velocities

The gas hold-up correlation to be used depends on the hydrodynamic regime. The homogeneous regime is encountered at low gas velocity and is characterised by a narrow bubble size distribution and by a radially uniform gas hold-up, see figure 2.1. As a consequence, variables do not change in the radial direction, so the gas hold-up can be obtained from the relative (or slip) velocity of the phases.

$$v_{21} = \frac{U_{gas}^{sup}}{\alpha} - \frac{U_{liq}^{sup}}{1-\alpha} \tag{2.6}$$

with v_{21} the slip velocity, U_{liq}^{sup} and U_{gas}^{sup} are the superficial liquid and gas velocities, respectively and α is the gas hold-up. The relation between the slip velocity v_{21} and

Table 2.1: Richardson & Zaki-exponent n as a function of the Reynolds number

Re	n
Re < 0.2	4.65
0.2 < Re < 1	4.35 $\mathrm{Re}^{-0.03}$
1 < Re < 500	4.45 $\mathrm{Re}^{-0.1}$
Re > 500	2.39

the slip velocity of a single bubble, v_∞, and can be written by the empirical relation

of Richardson & Zaki [Akker, 2000].

$$\frac{v_{21}}{v_{\infty}} = (1-\alpha)^{n-1} \tag{2.7}$$

The riser gas fraction and superficial gas and liquid velocities are coupled via

$$(1-\alpha_r)\, U^{sup}_{gas,r} - \alpha_r U^{sup}_{liq,r} = v_{\infty}\alpha_r\,(1-\alpha_r)^n \tag{2.8}$$

where $U^{sup}_{gas,r}$ and $U^{sup}_{liq,r}$ standing for the superficial gas and liquid velocities in the riser, respectively. The coefficient n is a function of the bubble-Reynolds number and is equal to 2.39 for the present bubbles, because the Reynolds number is 600. The values for n are given in table 2.1.

Chapter 3

Two-phase flow modeling

In this chapter, the basics of the two-phase flow in the airlift loop reactor are explained. Also the background of the $k - \epsilon$ turbulence model and the numerical simulation of dispersed multiphase flow in Fluent is discussed.

3.1 Two-phase flow

The phases of a multiphase flow can be any combinations of liquids, gases or solids. In this thesis there is a multiphase flow of two phases, namely a liquid ($_{liq}$) and a gas ($_{gas}$) phase.
According to literature e.g. [Sokolichin et al., 1997] there are essentially two basic approaches to dynamic flow simulations of dispersed two-phase flow. The first is an approach where both the liquid and the gas phase are represented in the Eulerian representation and thus referred to as Euler-Euler approach. The second approach treats only the liquid phase motion in the Eulerian representation and computes the motion of the dispersed gas phase fluid element in a Lagrangian way by individually tracking them on their way through the reactor. This approach has been termed Euler-Lagrange.
Only the Euler-Euler approach will be used in this thesis, because the Euler-Euler method is usually preffered when high superfial gas velocity with many bubbles is used on a large scale, which results in high gas hold-up and turbulence [Pan and Dudukovic, 2000].

3.1.1 Euler-Euler

The Euler-Euler model is one possible approach to dynamic flow simulations of two-phase gas-liquid flows. It assumes that each element of finite volume of the space domain contains a respective fraction (1-α) of the continuous and α of the dispersed phase.

The minimum size of a volume element must be substantially larger than a single dispersed bubble, because the volume fractions are considered to be constant within a volume element over a certain time step. Its size must, on the other hand, be small with respect to the dimension of the apparatus considered. The Euler-Euler two-phase model consists of a set of two momentum and continuity equations derived from a phase-weighted averaging process. The following assumptions are made [Sokolichin, 1994]:

- Isothermal conditions, hence the energy balances are not needed
- Only bubbles of one bubble size are generated with constant mass, that means that bubble coalescence and break up is neglected
- Constant liquid density
- Coupling between the two phases will be described through an interaction force term

The mass balance for phase k (continuous: $k = 1$, dispersed: $k = 2$) reads as

$$\frac{\partial}{\partial t}\alpha_k \rho_k + \nabla \cdot \left(\alpha_k \rho_k \vec{U}_k\right) = 0 \tag{3.1}$$

with α_k the volume fraction, ρ_k the density and $\vec{U}_k$ the mean velocity of each phase. The momentum equation for phase k is given by

$$\rho_k \alpha_k \frac{\partial \vec{U}_k}{\partial t} + \nabla \cdot \left(\alpha_k \rho_k \vec{U}_k \vec{U}_k\right) = -\alpha_k \nabla P + \rho_k \alpha_k \vec{g} - \nabla \cdot \alpha_k \left(\bar{\bar{\tau}}_{Re} - \bar{\bar{\tau}}_{mol}\right) + \vec{F}_w \tag{3.2}$$

with $\vec{g}$ the acceleration due to gravity, P the mean pressure of phase 1 and $\vec{F}_w$ the interfacial momentum transfer between the primary and secondary phase. This interfacial transfer is the most important characteristic of the multiphase flow and will be discussed in the following section. τ_{Re} is the Reynolds stress tensor and is defined as:

$$\tau_{Re} = \left\langle \rho_k \vec{U}'_k \vec{U}'_k \right\rangle_k \tag{3.3}$$

with $\vec{U}'_k$ the fluctuating part of the velocity and $< . >_k$ denotes the averaging operator associated to phase k. The Reynolds stress tensor will be discussed in section 3.2. $\bar{\bar{\tau}}_{mol}$ is the moluculair stress tensor and can be written as:

$$\bar{\bar{\tau}}_{mol} = 2\mu_k \vec{\vec{S}}_k - \frac{2}{3}\mu_k \nabla \cdot \vec{U}_k \vec{\vec{I}} \tag{3.4}$$

with μ_k the dynamic viscosity, $\vec{\vec{I}}$ the unity tensor and $\vec{\vec{S}}_k$ the rate of strain tensor

$$\vec{\vec{S}}_k = \frac{1}{2}\left(\nabla \vec{U}_k + (\nabla \vec{U}_k)^T\right) \tag{3.5}$$

To close equation 3.1 and 3.2 a third equation is needed:

$$\sum_{k=1}^{2} \alpha_k = 1 \tag{3.6}$$

3.1.2 Interfacial Momentum Transfer

In dispersed liquid-gas phase flow, bubbles are assumed to interact only slightly with each other, because the most bubbles have only interaction with the liquid phase. Therefore, the momentum interfacial transfer terms in the basic equations can be obtained from the analysis of the local balance of forces acting on an isolated bubble. Shear stress and gravity are the main forces acting on a bubble in a liquid. However, there is nearly always a relative motion between the liquid and the bubble. The liquid flow around individual bubbles leads to local variations in the pressure and shear stress, the resulting interaction forces: F_w. Due to these variations, the F_w have to be approximated through more or less empirical correlations. In general, three different contributions are taken into account: drag force F_d, virtual mass effects, F_{vm} and a lift force F_l, leading to the following approximation for the force of interaction:

$$F_w = F_D + F_{vm} + F_l \tag{3.7}$$

The three contributions of F_w will be briefly discussed in the following subsections.

Drag Force

The drag force is the force between the liquid and the bubbles in an uniform flow field under non-acceleration conditions. A bubble that moves relative to a liquid accelerates part of the liquid around it and is in turn slowed down by the surrounding liquid. The drag force is a consequence of the liquid surrounding the bubble, which result in shear and a pressure difference. It is the dominant force and is often the only one considered. Generally the equation of the drag force can be written as:

$$F_D = K_{21} U_r \tag{3.8}$$

Here K_{21} denotes the interphase momentum exchange coefficient which represents the drag between the two phases, U_r is the averaged value of the local relative velocity between each bubble and the surrounding fluid. Most of the models used for the exchange coefficient [Simonin, 1997]; [Mudde and Simonin, 1999] are based on the model of Schiller and Naumann [Fluent Inc., 1998]:

$$K_{21} = \frac{3}{4} C_D \alpha \frac{|U_{liq} - U_{gas}|}{d_{gas}^2} \tag{3.9}$$

in which d_{gas} is the bubble diameter and the drag function C_D, is described as:

$$C_D = \frac{24}{Re_{gas}} (1 + 0.15 Re_{gas}^{0.687}) \qquad Re_{gas} \leq 1000 \tag{3.10}$$

When $Re_{gas} > 1000$, $C_D = 0.44$.
This model is originally mend for an isolated solid particle in a flow and does not take into account the deformation of a bubble. In this study the model of [Schwarz and Turner, 1988] is used. The exchange coefficient is here defined as:

$$K_{21} = (1 - \alpha) \alpha C_w \tag{3.11}$$

with $C_w = 5 \cdot 10^4\ kgm^{-3}s^{-1}$.

The average value of the local relative velocity between each bubble and the surrounding liquid ($\overrightarrow{U}_r$) of equation 3.8 can be described as:

$$\overrightarrow{U}_r = \left(\overrightarrow{U}_{gas} - \overrightarrow{U}_{liq}\right) - \overrightarrow{U}_d \tag{3.12}$$

with $\left(\overrightarrow{U}_{gas} - \overrightarrow{U}_{liq}\right)$ denoting the mean slip velocity and $\overrightarrow{U}_d$ a drifting velocity due to correlation between the distribution of the particles and the turbulent fluid motions. The drift velocity takes into account the dispersion of the particles due to transport by turbulent fluid motion. This velocity is calculated by [Lathouwers, 1999] with:

$$\overrightarrow{U}_d = -D_{12}^t \left(\frac{1}{\sigma_{21}\alpha}\nabla\alpha - \frac{1}{\sigma_{21}(1-\alpha)}\nabla(1-\alpha)\right) \tag{3.13}$$

with the turbulent Schmidt number $\sigma_{21} = 0.67$ as default value and the binary diffusion tensor D_{12}^t described as a function of the covariance tensor between the turbulent velocity fluctuations of the two phases and a bubble turbulent characteristic time, τ_{12}^t:

$$D_{12}^t = \frac{1}{3}\tau_{12}^t \left\langle \overrightarrow{U}'_{liq} \overrightarrow{U}'_{gas} \right\rangle_{gas} \tag{3.14}$$

with $\overrightarrow{U}'$ the fluctuating part of the velocity component of the gas and liquid phase. In practice, the dispersion tensor is limited to its diagonal part.

Virtual Mass Effect

One of the additional internal momentum sources is the added mass force. The added mass force occurs when the secondary, dispersed phase accelerates relative to the primary phase. So, if the bubbles are accelerated relative to the liquid part the surrounding liquid has to be accelerated as well. This exerts a virtual mass force on the bubble. The virtual mass effect is calculated by [Fluent Inc., 1998] with:

$$F_{vm} = \alpha\rho_{liq}C_{vm}\left(\frac{D_{liq}\overrightarrow{U}_{liq}}{Dt} - \frac{D_{gas}\overrightarrow{U}_{gas}}{Dt}\right) \tag{3.15}$$

where the coefficient C_{vm} corresponds to the volume of liquid which is accelerated with the bubble. A number of different correlations can be found for C_{vm} in literature. For low volume fraction of the dispersed phase $C_{vm} = 0.5$ is a common value. Simonin et al. ([Simonin and Viollet, 1990], [Simonin, 1990]) use an other expression for the virtual mass in which the drifting velocity $\overrightarrow{U}_d$, (see the previous section) is included. The fluctuations due to the turbulent fluid motions, incorporated in the drifting velocity are not taken into account in equation 3.15.
The virtual mass effect can be significant when the secondary density is much smaller than the primary phase density. Typical examples comprise the flow fields at the upper and lower end of a loop reactor.

Lift Force

Another additional internal momentum source is the lift force on the secondary phase. This lift force acts on the bubble mainly due to velocity gradients in the primary phase flow field. The velocity gradients will induce an additional force, perpendicular to the main flow direction. The lift force acting on a secondary phase in a primary phase can be approximated by [Thomas et al., 1983] with:

$$F_l = -\alpha \rho_{liq} C_l \left(\overrightarrow{U}_{gas} - \overrightarrow{U}_{liq} \right) \times \left(\nabla \times \overrightarrow{U}_{liq} \right) \tag{3.16}$$

The lift force can also be referred to as 'Magnus force', so C_l is the Magnes force constant. The value for the constant has been calculated by [Auton, 1983] and was found to be equal to 0.53. The lift force will be more significant nearby the walls, where the velocity gradients are relatively large in bubble reactors.

When a flat geometry of a reactor is implement in 3D simulation of the described airlift, the lift force pushes the gas flow against the front and back wall in numerical calculations. This behaviour has not been observed during experiments and seems not realistic. So, the lift force is not taken into account in the simulations.

3.2 Turbulence modeling

Modeling of turbulent flow requires appropriate modeling procedures to describe the effects of the turbulent fluctuations of velocity and scalar quantities on the basic conservation equations. In a turbulent flow the advective, non-linear term of the momentum equation is dominating the diffusive term. Turbulent flows have several typical characteristics which are different from laminar flows. A turbulent flow has a macro and a micro structure with their own length, time and velocity scales. So, the mass and momentum balance combined with the appropriate boundary conditions are sufficient to compute any flow field provided that an adequate resolution for the smallest scales is used. This means that the cells should be at least as small as the smallest length scale in the flow field. The smallest scale is given by the Kolmogorov length:

$$\lambda = \left(\frac{\nu^3}{\epsilon} \right)^{\frac{1}{4}} \tag{3.17}$$

where λ is the Kolmogorov length scale and ϵ the turbulent energy dissipation. The total number of scales in the three dimensional domain can be written as:

$$N_t \propto \left(\frac{L}{\lambda} \right)^3 \tag{3.18}$$

The number of cells, N_t needed scales with $Re^{\frac{9}{4}}$, because $\frac{\lambda}{L} \propto Re^{-\frac{3}{4}}$. The computational effort is extremely high even at moderate Reynolds numbers. Therefore, turbulence models are used to predict turbulent flow.
There are several approaches for simulating turbulent flow, the Reynolds Averaged

Navier-Stokes (RANS), Large Eddy Simulation (LES) and Direct Numerical Simulations (DNS), the latter obviously only applicable to relatively low Reynolds numbers and simple geometries. Only the RANS approach for simulating turbulent flow is used and described in this thesis. See for example [Ferziger and Peric, 1999] for more information about LES and DNS.

3.2.1 Reynolds Average Navier-Stokes (RANS)

In the RANS method every variable of a statistically steady flow can be written as a sum of a time averaged value and a fluctuation part: the velocity at a point can be written in this way:

$$U_i = \overline{U_i} + U_i' \tag{3.19}$$

where $\overline{U_i}$ is the time averaged value of U_i defined by [Merk, 1980] as:

$$\overline{U_i} = \lim_{T\to\infty} \frac{1}{T} \int_0^T U_i dt \tag{3.20}$$

Here t is the time and T is a time scale. This time scale must be large compared to the typical time scale of the turbulence fluctuations. From equation 3.20 it follows that $\overline{U_i'} = 0$. From a quadratic non-linear term we get two terms, the product of the average and a covariance, e.g.:

$$\overline{UU} = \overline{U}\,\overline{U} + \overline{U'U'} \tag{3.21}$$

The last term is zero only if the two quantities are uncorrelated. This is not the case in the two-phase and turbulent one-phase flows, so the conservation equations contain terms such as $\rho\overline{U'U'}$, called the Reynolds stress. Substituting expressions of this kind in the basic momentum balance yields the Reynolds-averaged momentum equation (equation 3.2) for predicting turbulent flows. The presence of this term implies that the equations are not closed. So, this method requires the introduction of further modeling, these are called the turbulence model.

Fluent relates the Reynolds stresses to mean flow quantities via one of three turbulence models:

- the $k - \epsilon$ model
- the Differential Reynolds Stress Model (RSM)
- the Re-Normalization Group (RNG) $k - \epsilon$ model

The $k - \epsilon$ model is described in the following section. The other models are not described in this thesis, because only the $k - \epsilon$ model is used. The $k - \epsilon$ model reproduces a more realistic dispersion effect of the bubbles, because the two-phase additions to the turbulence model (see section 3.2.3) have been originally developed for the $k - \epsilon$ model.

3.2.2 $k-\epsilon$ one-phase Model

The $k-\epsilon$ model is an one-phase eddy-viscosity model in which the Reynolds stresses are assumed to be proportional to the mean velocity gradients. This assumption is known as the Boussinesq hypothesis and provides the following expression for the Reynolds stresses:

$$\rho\overrightarrow{U_i'U_j'} = \rho\frac{2}{3}\left(k+\nu_t\nabla\cdot\overrightarrow{U}\right)\overrightarrow{I} - \mu_t\left(\nabla\overrightarrow{U}+\left(\nabla\overrightarrow{U}\right)^T\right) \tag{3.22}$$

$\nu_t = \mu_t/\rho$ and k is the turbulent kinetic energy:

$$k = \frac{1}{2}\sum_i \overline{U_i'U_i'} \tag{3.23}$$

The turbulent viscosity, μ_t, plays the same role as the molecular viscosity μ. Therefore, the form of the Reynolds averaged momentum equations remains identical to the form of the laminar momentum equations except that μ is replaced by an effective viscosity, μ_{eff}:

$$\mu_{eff} = \mu + \mu_t \tag{3.24}$$

The turbulent viscosity μ_t is given by:

$$\mu_t = \rho C_\mu \frac{k^2}{\epsilon} \tag{3.25}$$

where ϵ is the turbulent energy dissipation and C_μ a representing modeling constant.

The values of k and ϵ required in equation 3.25 are obtained by the following conservation equations.

$$\rho\frac{\partial k}{\partial t} + \frac{\partial}{\partial x_i}(\rho U_i k) = \frac{\partial}{\partial x_i}\left[\left(\frac{\mu_t}{\sigma_k}\right)\frac{\partial k}{\partial x_i}\right] + G_k - \rho\epsilon \tag{3.26}$$

$$\rho\frac{\partial \epsilon}{\partial t} + \frac{\partial}{\partial x_i}(\rho U_i \epsilon) = \frac{\partial}{\partial x_i}\left[\left(\frac{\mu_t}{\sigma_\epsilon}\right)\frac{\partial \epsilon}{\partial x_i}\right] + C_{1\epsilon}\frac{\epsilon}{k}G_k - C_{2\epsilon}\rho\frac{\epsilon^2}{k} \tag{3.27}$$

In this $C_{1\epsilon}$ and $C_{2\epsilon}$ are empirical constants, σ_k and σ_μ are the turbulent Prandtl numbers for k and ϵ respectively. The values of this empirical constants are written in table 3.1.

Table 3.1: The values of the empirical constants

Constant	$C_{1\epsilon}$	$C_{2\epsilon}$	C_μ	σ_k	σ_ϵ
Values	1.44	1.92	0.09	1.0	1.3

G_k is the rate of production of turbulent kinetic energy due to velocity gradients:

$$G_k = \mu_t\left(\frac{\partial U_j}{\partial x_i} + \frac{\partial U_i}{\partial x_j}\right)\frac{\partial U_i}{\partial x_i} \tag{3.28}$$

The $k-\epsilon$ model is originally developed for single phase steady flow and is restricted by some assumption. One of the assumption of this model is that the flow is fully turbulent and that the flow is close to a solid wall [Launder and Spalding, 1974]. This means that the turbulent viscosity is modeled only for high Reynolds numbers. Often the $k-\epsilon$ model is used for multiphase flow with no regard of the influence of the second phase. This influence can be modeled through additional terms that includes interphase turbulent momentum transfer, see the next section.

3.2.3 Dispersed Turbulence Model

The dispersed turbulence model is one of the two methods for modeling turbulence in multiphase flows within the context of the $k-\epsilon$ model in Fluent. In this model, inter particle collisions are negligible and the dominant process in the random motion of the secondary phase is the influence of the primary-phase turbulence. Fluctuation of the secondary phase can therefore be given in terms of the primary phase. The conditions, for which the dispersed turbulence model is valid, are:

- The number of phases is limited to two: the continuous (primary) phase and the dispersed (secondary) phase
- The secondary phase must be dilute.

Turbulence in the Continuous Phase

Turbulence predictions for the continuous phase are obtained using the standard $k-\epsilon$ model supplemented with extra terms that include the interphase turbulent momentum transfer. The turbulent eddies of the continuous phase have a characteristic time (τ^t_{liq}) and length scale (L^t_{liq}) as:

$$\tau^t_{liq} = \frac{3}{2} C_\mu \frac{k_{liq}}{\epsilon_{liq}} \tag{3.29}$$

$$L^t_{liq} = \sqrt{\frac{3}{2}} C_\mu \frac{k_{liq}^{\frac{3}{2}}}{\epsilon_{liq}} \tag{3.30}$$

Two phase flow turbulence models are obtained by multiplying the single phase flow transport equations of k and ϵ (equation 3.26 and 3.27) with the void fraction, $(1-\alpha)$, and adding of two-phase flow terms. The use of the single phase equations is probably not totally justified but so far no better alternative has been developed.

$$\frac{\partial}{\partial t}((1-\alpha)\rho k) + \nabla\cdot\left((1-\alpha)\rho\vec{U}_{liq}k\right) = \nabla\cdot\left((1-\alpha)\rho\frac{\mu^t}{\sigma_k}\nabla k\right) + (1-\alpha)\rho(P-\epsilon) + (1-\alpha)\rho\Pi_{k_{liq}} \tag{3.31}$$

$$\frac{\partial}{\partial t}((1-\alpha)\rho\epsilon)+\nabla\cdot((1-\alpha)\rho\vec{U}_{liq}\epsilon) = \nabla\cdot\left((1-\alpha)\rho\frac{\mu^t}{\sigma_k}\nabla\epsilon\right)+(1-\alpha)\rho\frac{\epsilon}{k}\left(C_{1\epsilon}P - C_{2\epsilon}\epsilon\right)+(1-\alpha)\rho\Pi_{\epsilon_{liq}} \tag{3.32}$$

$\Pi_{k_{liq}}$ and $\Pi_{\epsilon_{liq}}$ are the additional terms representing the influence of the dispersed phase on the continuous phase. All other terms have the same meaning as in the single phase $k-\epsilon$ model. The term $\Pi_{k_{liq}}$ takes the following form:

$$\Pi_{k_{liq}} = \frac{K_{21}}{(1-\alpha)\rho_{liq}}(< U'_{liq,i}U'_{gas,i} > - < U'_{liq,i}U'_{liq,i} > +(U_{gas,i} - U_{liq,i})\cdot U_{d,i}) \tag{3.33}$$

which can be simplified to:

$$\Pi_{k_{liq}} = \frac{K_{21}}{(1-\alpha)\rho_{liq}}(k_{12} - 2k_{liq} + (\vec{U}_{gas} - \vec{U}_{liq})\cdot overrightarrowU_d) \tag{3.34}$$

where k_{12} is the covariance of the continuous and dispersed phase velocities. $\Pi_{\epsilon_{liq}}$ is modeled according to [Elghobashi and Abou-Arab, 1983]:

$$\Pi_{\epsilon_{liq}} = C_{3\epsilon}\frac{\epsilon_{liq}}{k_{liq}}\Pi_{k_{liq}} \tag{3.35}$$

where $C_{3\epsilon}$=1.2.

Turbulence in the Dispersed Phase

Turbulence predictions in the dispersed phase are made by an extension of Tchen's theory of dispersion of discrete particles by homogeneous and steady turbulent fluid motions [Simonin and Viollet, 1990]. Time and length scales that characterize the motion are used to evaluate dispersion coefficients, correlation functions, and the turbulent kinetic energy of the dispersed phase.

The characteristic particle relaxation time, connected with inertial effects acting on the particle phase, is defined as

$$\tau_{21}^F = \alpha\rho_{gas}K_{21}^{-1}\left(\frac{\rho_{gas}}{\rho_{liq}} + C_{vm}\right) \tag{3.36}$$

The Lagrangian integral time scale calculated along particle trajectories is defined as

$$\tau_{21}^t = \tau_{liq}^t\left(1 + C_\beta\xi^2\right)^{-\frac{1}{2}} \tag{3.37}$$

where

$$\xi = \frac{|\vec{U}_{gas} - \vec{U}_{liq}|\tau_{liq}^t}{L_{liq}^t} \tag{3.38}$$

and

$$C_\beta = 1.8 - 1.35cos^2\theta \tag{3.39}$$

θ is the angle between the mean particle velocity and the mean relative velocity. The ratio between these two characteristic times is written as

$$\eta_r = \frac{\tau_{21}^t}{\tau_{21}^F} \tag{3.40}$$

Following Simonin, the turbulence quantities for the dispersed phase can be written as follows

$$k_{gas} = k_{liq}\left(\frac{b^2+\eta_r}{1+\eta_r}\right) \tag{3.41}$$

$$k_{12} = 2k_{liq}\left(\frac{b+\eta_r}{1+\eta_r}\right) \tag{3.42}$$

$$D_{21}^t = \frac{1}{3}k_{12}\tau_{21}^t \tag{3.43}$$

$$b = (1+C_{vm})\left(\frac{\rho_{gas}}{\rho_{liq}}+C_{vm}\right)^{-1} \tag{3.44}$$

where $C_{vm} = 0.5$ is the added-mass coefficient.

3.3 Computational fluid dynamics

The non-linearity of equation 3.2 makes it impossible to solve the mass and momentum balance directly, given a set of boundary conditions. In order to solve the balances the first step is to derive their discretised forms which can be implemented in the numerical procedure. The CFD packaged used in this study uses the finite volume concept. The control volume based technique is used to solve the conservation equations for mass, momentum and turbulence quantities. This control volume based techniques consists of:

- Division of the domain into discrete control volumes using a grid
- Integration of the equations on the individual control volumes to construct the algebraic equations for discrete unknowns
- Solution of the discretised equations

The accuracy of the discretisation is determined by the size of control volumes. The discretisation of the differential equations is described in this section.

3.3.1 First-order upwind

The first-order upwind scheme sets the value at the cell face to be the upstream cell-center value. This means that if a cell face value is needed the value of the cell upwind is used. This scheme provides stability for the discretisation of the pressure correction equation, and gives good results for convective dominated flows.

3.3.2 Power Law

The power law interpolation scheme interpolates the flux of a variable ϕ using the exact solution to an one-dimensional convection diffusion equation:

$$\frac{d}{dx}(\rho u\phi) = \frac{d}{dx}\Gamma\frac{d\phi}{dx} \tag{3.45}$$

where Γ and ρu are constant. This equation can be integrated to yield the following solution describing how ϕ varies with x over an interval L:

$$\frac{\phi(x) - \phi_0}{\phi_L - \phi_0} = \frac{exp\left(Pe\frac{x}{L}\right) - 1}{exp(Pe) - 1} \tag{3.46}$$

where Pe is the Peclet number

$$Pe = \frac{\rho u L}{\Gamma} \tag{3.47}$$

The power low interpolation scheme interpolates at high Peclet numbers, when the flow is dominant by convection, equivalent to a first order upwind scheme.

In general, the power law scheme is more stable compared to the higher order schemes and, for the same grid size, less computationally intensive. However, the higher-order scheme need fewer grid points for a required degree of accuracy, compared to the power law scheme.

3.3.3 Quadratic Upwind Interpolation (QUICK)

Higher order schemes are alternatives for the power-law scheme. These schemes provide higher numerical accuracy, but numerical instabilities may occur. The QUICK

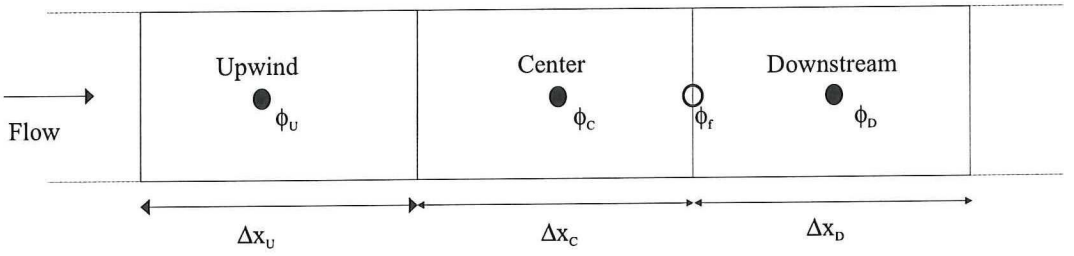

Figure 3.1: Central, Downstream and Upwind cell nomenclature employed in the higher order interpolation schemes

scheme involves a quadratic interpolation and is based on a weighted average of second-order upwind and central interpolations of the face-variable. The face value

can be written in terms of the neighbor values as:

$$\phi_f = (1-\theta)\left[\frac{\Delta x_U - 2\Delta x_C}{\Delta x_U + \Delta x_C}\phi_C - \frac{\Delta x_C}{\Delta x_U + \Delta x_C}\phi_U\right] + \theta\left[\frac{\Delta x_D}{\Delta x_C + \Delta x_D}\phi_C - \frac{\Delta x_C}{\Delta x_C + \Delta x_D}\phi_D\right] \tag{3.48}$$

where Δx_U, Δx_C and Δx_D are the cell size of U, C and D, respectively. Equation 3.48 computes the face value with second or third order accuracy, depending upon the choice of θ. $\theta = 1$ results in a central second-order interpolation, while $\theta = 0$ yields a second-order upwind value. The third-order upwind needs a $\theta = \frac{2}{3}$ and the traditional QUICK scheme is obtained by $\theta = \frac{3}{4}$. Second-order central difference will yields oscillations at discontinuities and second-order upwind or QUICK will produce undershoots and overshoots. Linear combinations of the methods can produce a scheme which is both stable and accurate.

The power law is used in all the simulations which are done. This is not the most accurate one as is written by [Loncle, 2000]. For further discussion see Loncle.

3.3.4 Time-Dependence

In transient simulations besides the spatial discretisation also a time discretisation is needed. Temporal discretisation involves the integration of every term in the differential equations over a time step Δt. The integration of the transient terms is straightforward

$$\int_t^{t+\Delta t} \frac{\partial(\rho\phi)}{\partial t} dt = (\rho\phi)^{t+\Delta t} - (\rho\phi)^t \tag{3.49}$$

where ϕ is the conserved quantity. The integration of the other terms in the conservation equations, e.g., convection terms such as $\rho u\phi$, requires an assumption about how $\rho u\phi$ varies with time from t to t+Δt. Here, a first order implicit method is used:

$$\int_t^{t+\Delta t} (\rho u\phi) dt = (\rho u\phi)^{t+\Delta t}\Delta t \tag{3.50}$$

The advantage of the fully implicit scheme is that it is unconditionally stable. But one must be careful with stable scheme, that allow a very large time-step, but leaves an inaccuracy proportional to Δt, which is also large.

3.3.5 Solution Procedure

Each iteration consists of the steps which are illustrated in figure 3.2. These steps are outlined below.

1. The momentum equations are each solved in turn using values for pressure in order to update the velocity field. First the primary phase equations are solved and then the secondary phase.

2. The pressure correction equation is then solved to obtain the necessary corrections to the pressure field such that continuity of both phases are achieved.
3. The physic volume fractions are calculated and updated.
4. The k and ϵ equations are solved using the updated velocity field.
5. Other equations are solved using the previously updated values of the other variables.
6. A check for convergence of the equation set is made.

These steps are continued until the error has decreased to a required value or a finite number of iteration steps has been reached.

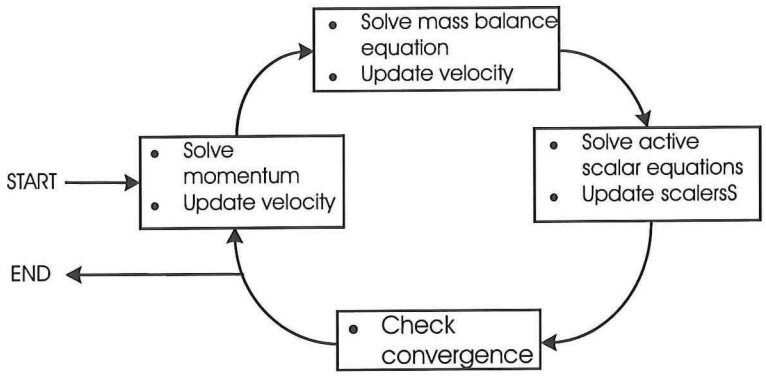

Figure 3.2: Overview of the Solution Procedure

Chapter 4

Computational Setup

4.1 General Information

All simulations have been carried out with the commercial CFD package Fluent, version 4.5.6. Fluent 5 was not used because the Eulerian Multiphase Model is not implemented in it.

The model described in section 3.1 is solved using the procedure described in section 3.3.5. The steady-state solution is considered converged when the sum of the normalised residuals for each time step has dropped below $1 \cdot 10^{-3}$ in one iteration step.

The Line-Gauss-Siedel (LGS) solution technique was used for all parameters. To achieve the convergence the underrelaxion factor for pressure was 0.5, for the liquid and gas velocities, volume fraction, viscosity and the turbulence quantities k and ϵ it was set on 0.2 and for the body forces at 1. The smaller the factor the heavier is the degree of underrelaxion and the greater is the degree of control exercised over the change permitted from one iteration to the next.

4.2 Grid

For the 3D simulations with one symmetry axis the physical domain of the airlift (x $\times$ y $\times$ z), with x the width, y the depth and z the height of the airlift, is discretised into a structured grid of 16 $\times$ 10 $\times$ 80 cells. The riser and downcomer consist of 6 and 10 cells, respectively in the x direction and the internal wall begins at cell 10 and ends on cell 60 in the z-direction. The grid is shown in appendix C. For the simulations of the quarter part of the airlift loop reactor the physical domain is discretised into a structured grid of 16 $\times$ 6 $\times$ 80 cells, so the x and z direction are the same as the previous one.

4.2.1 Boundary Conditions

To solve the discretised equations using the finite volume method, boundary conditions have to be specified for each cell type, which are shown in figure 4.1.

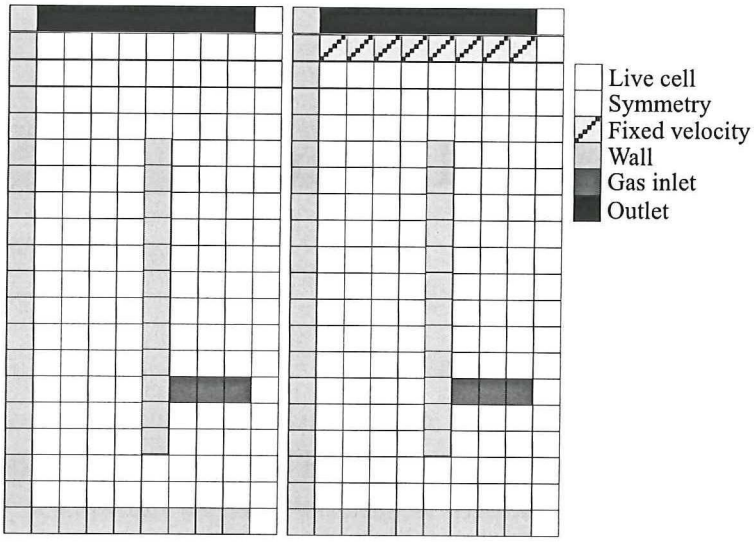

(a) free outlet surface

(b) fixed velocities just below the outlet

Figure 4.1: Boundary conditions (a) with free surface on the outlet (b) with fixed velocities just below the outlet

In the following sections the different types of cells will be discussed.

4.2.2 Inlet

The boundary conditions at the gas inlet are set by prescribing a fixed inlet velocity of U_z=0.25 m/s and a given gas fraction of α. The gas fraction is varied from 1.2% to 10% at the inlet of the airlift. The gas flow rate can be calculated with the help of the surface of the gas inlet. For the water phase all velocities are set to zero at the sparger. The inlet conditions for the turbulence quantities, the turbulence intensity and characteristic length are set on 10 % and 1 m, respectively. It should be remarked, that these inlet values only influence the final solution via the diffusion term in the k_1 and ϵ balances, since at the inlet the convective terms are zero, because the liquid velocity in the inlet is zero. The sparger is made of several aerating 'strips' separated by flow channels. Five possibilities are tried and three of them are shown in figure 4.2. In figure 4.3 the 3 dimensional gas inlet is shown.

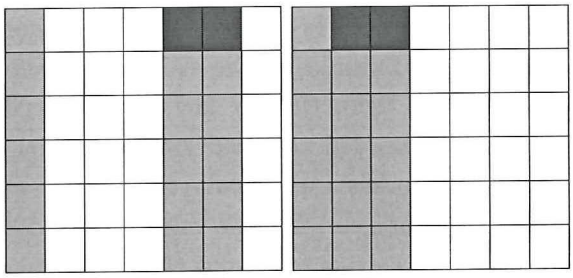

(a) channel at wall (b) sparger at wall

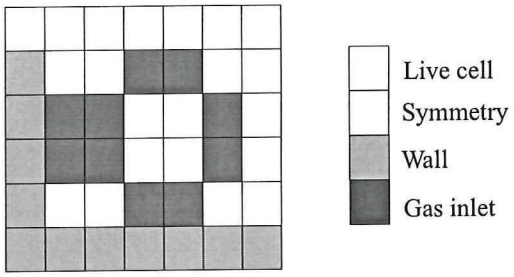

(c) checkerboard sparger

Figure 4.2: Difference inlet geometries (a) side view of channel at wall (b) side view of sparger at wall (c) top view of checkerboard sparger

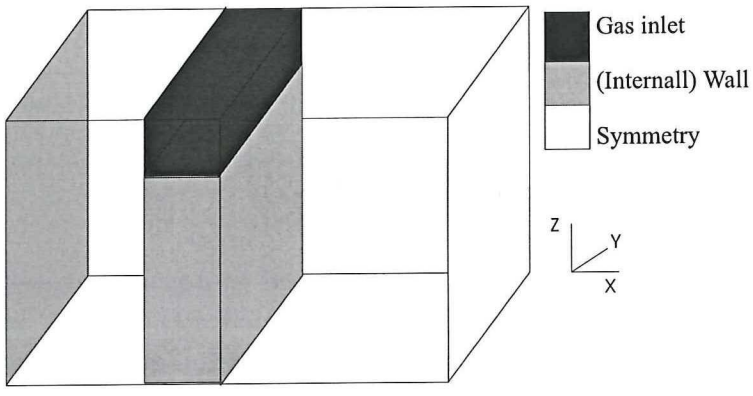

Figure 4.3: 3-Dimensional gas inlet of the sparger closest to the center

4.2.3 Wall

Wall functions are used at the grid points near the wall to estimate the effect of the wall on the flow. The wall functions are based on the assumption that a fully developed equilibrium turbulent boundary layer exists. Therefore, all the relevant flow properties can be obtained from the log law, that describes such boundary layers. Wall functions provide a needed near-wall closure model for the $k-\epsilon$ model and the standard RSM. These models are not valid in the near-wall region (y^* <30), which is the dimensionless wall distance. It has a value around 500 in the simulations done. Therefore, just adding more grids to resolve the turbulent boundary layer can lead to better predictions, but the number of grid cells had to be not too high. This has led to the development of the so-called low-Reynolds number $k-\epsilon$ models. Such models provide empirically based near-wall modifications which lack universality and often exhibit convergence difficulties.

Fluent provides two wall function options for turbulent flows:

- the standard wall function
- the nonequilibrium wall function

When the underlying assumption of an equilibrium turbulent boundary layer is satisfied the standard wall function approach works well, in contrast with the situation when the boundary layer is subject to significant pressure gradients, or near stagnation and re-attachment points, or in regions of high curvature. In such situations the standard wall function performs poorly and the nonequilibrium wall function can improve the accuracy of such predictions. Both wall functions are based on one phase flow and in this research the wall functions were used for two-phase flow. So, the use of the wall function are not totally correct in this thesis, but no other wall functions are present for two-phase flow. The wall functions are described in appendix D

4.2.4 Outlet

For the outlet boundary two approach are used.

I The outlet boundary condition is approached as a gas disengagement space patched at the top of the airlift. This is a perfectly 'natural' and realistic scenario that allows the liquid to expand and reach a quasi-steady state. The disadvantage is that the relation for K_{21} (see equation 5.8) is not valid in the air area. Therefore, it is not possible to simulate the diffusion part of the equation 3.2. In this simulations it will be neglected.

II In the second approach the outlet is defined as a fixed velocity inlet. In the cell row beneath the top-row, the normal velocities are fixed: $U_{z,1} = 0$ m/s and

$U_{z,2} = 0.2$ m/s, which is the assumed slip velocity. As a result the primary phase is prevented to flow out of the airlift. In this way the volume of the liquid phase is also fixed in the total domain, which is a disadvantage of this approach.

4.3 Physical Constants

The physical constants used in the simulations are summarized in table 4.1.

Table 4.1: Physical constants used in simulation

		Density [kg· m^{-3}]	Dynamic viscosity [kg· m^{-1}· s^{-1}]	Bubble diameter [1· 10^{-3} m]
Liquid	water	$1 \cdot 10^3$	$1 \cdot 10^{-3}$	-
Gas	air	1.2	1.72· 10^{-5}	3.0

Chapter 5

Results and Discussion

In this chapter 3-dimensional simulations of the airlift loop reactor, which is described in chapter 2, are presented to illustrate the influence of the sparger, gas inlet fraction, turbulence model, time step, symmetry axis and grid size. The results are compared to the outcome of a simple one dimensional mechanical energy balance and simulations which are done by [Mudde and Akker, 2001]. All simulations are performed using FLUENT.V4.5.6.
The solution is assumed to be in steady-state when in Fluent the sum of the normalised residuals for each time step has dropped below $1 \cdot 10^{-3}$ in one iteration step. This convergence is rather arbitrary. It is found that simulations with minimal residual sum of $1 \cdot 10^{-3}$ are not surely really convergent simulations, because when more time steps (simulation time 160 s) are simulated the convergent results are different from simulations with lesser time steps (simulation time 50 s). Furthermore, a minimal residual sum smaller than $1 \cdot 10^{-3}$ can lead to another steady-state. Simulations with smaller minimal residual sum needed more simulation time and are therefore not tested.

5.1 Basic simulation

The start up procedure of the different simulations is described in this section. Furthermore, the basic simulation will be described and discussed. All the results of the other simulations are compared with the results of the basic simulation.

5.1.1 Start up procedure

First the modeled airlift loop reactor is completely filled with water. Water is put into the reactor via the sparger with a vertical-velocity of 0.25 m/s. The water leaves the reactor through the outlet on the top of the reactor. Consequently, a water circulation is established in the airlift loop reactor. This circulation of the

liquid phase is an effective procedure for starting the simulations of the two-phase flow in an airlift loop reactor in Fluent.
When the liquid phase flow is stationair gas is putted into the reactor through the inlet sparger with a velocity of 0.25 m/s and the inlet velocity of water is fixed at zero. The gas leaves the reactor through the outlet just like water leaves the airlift at the begin of the simulation, until the 'free surface' is established. At this moment the simulation is (nearly) stationair and the water stays in the airlift loop reactor.

5.1.2 Results of the basic simulation

The first case will be used as the basis for all simulations, and is called the basic simulation. The standard set up of all the simulations are:

- Gas inlet velocity 0.25 m/s
- Gas inlet sparger is a kind of checkerboard (see chapter 4)
- Gas inlet fraction 3.6 % ($U^{sup}_{gas_{in}} = 0.45cm/s$)
- Grid size 16 x 6 x 80 (width x depth x height)
- Time step of $1 \cdot 10^{-3}s$
- Outlet of type II, i.e. the normal velocity of the gas and liquid phase are fixed at the outlet (see section 4.2.4)
- Only one quarter of the airlift is simulated
- Fixed gas and liquid vertical velocity at the outlet of 0.2 m/s and 0 m/s, respectively
- Drag force and virtual mass included
- Standard wall function
- The default material properties from table 4.1 are used
- Maximal residual sum $1 \cdot 10^{-3}$ for convergence

$U^{sup}_{gas_{in}}$ is the superficial inlet gas velocity (superficial gas velocity of the inlet gas fraction). This is not the same as the superficial gas velocity in the riser when the gas circulates through the airlift.

Figure 5.1 depicts the gas hold-up pattern in the airlift loop reactor 160 s after the onset of the aeration. The concentration of gas just above the sparger (k=20) is at the internal wall side larger than at the center of the riser. The gas is spread out further horizontally at higher place (k=40) in the riser of the airlift and the gas distribution is nearly homogeneous in the top of the riser (k=75). This is also shown

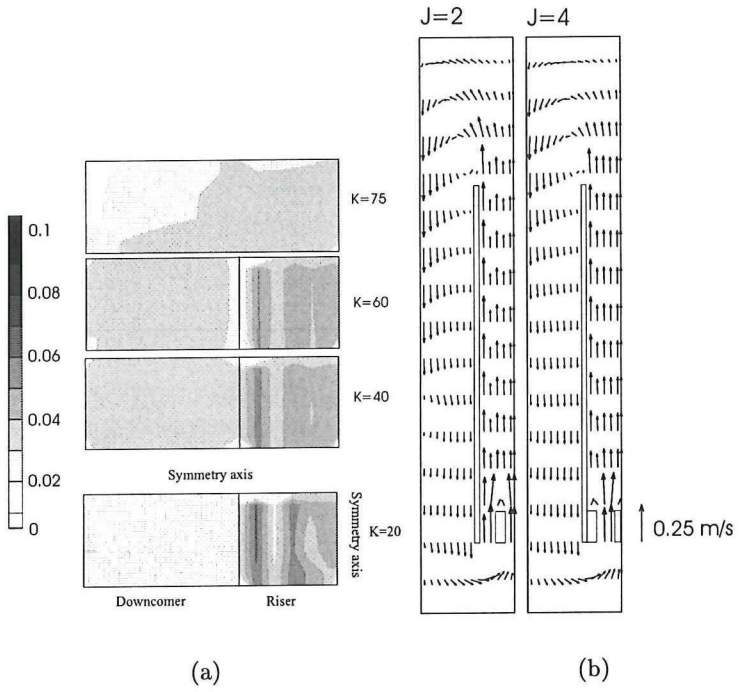

Figure 5.1: Gas fraction distribution and liquid velocity field for the basic simulation (a) the top view of the airlift at k=20, 40, 60 and 75 (b) the side view of the airlift loop reactor at j=2 and j=4

in figure 5.2 where the gas hold-up is plotted against the position in the x-direction of the riser. Here, the height of the peaks of the gas hold-up right above the gas inlet decreases more and more when the k-plane is higher in the airlift. The gas fraction has a nearly constant distribution in the top of the riser.
The gas flow out of the sparger near the wall is splitted in two straight lines, one against the internal wall and one a quarter in the x-direction of the total riser from the internal wall. In literature, [Mudde and Akker, 2001], the splitted gas flow is not found. The simulations of literature has the grid 44 x 14 x 104 (width x depth x hight) grid cells, which results in a smaller grid size. So, when the number of grid cells is doubled in our simulation the splitting is may not be found. This will be discussed further in section 5.8.
The gas hold-up just above the gas inlet in the center of the riser is very low in contrast with the gas hold-up above the other inlet part. Maybe a part of the gas out of the first inlet is going to the internal wall, which result in a lower gas hold-up in the center of the column and a higher gas hold-up near the internal wall. This is restored just higher in the riser.

The liquid and gas flow rate and the mean gas fraction in the riser and downcomer of this case are given in table 5.1. The downcomer gas fraction is very high at the gas flow rate used and is somewhat lower than the riser gas fraction. The high downcomer gas fraction can partly explain by the higher gas fraction near the

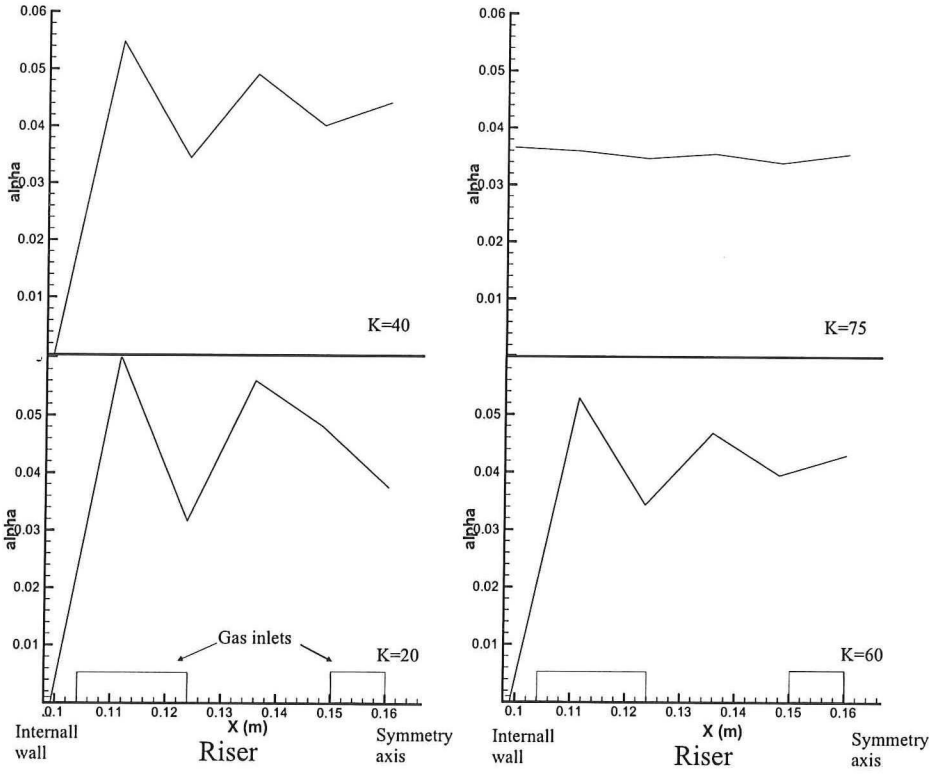

Figure 5.2: Gas hold-up distribution plotted against the position in the x-direction of the riser at different height of the airlift loop reactor

Table 5.1: Gas hold-up in the riser and downcomer and the liquid and gas flow for the basic simulation

	$\langle\alpha_r\rangle$ [%]	$\langle\alpha_d\rangle$ [%]	ϕ_{liq} $[\cdot 10^{-4} m^3/s]$	ϕ_{gas} $[\cdot 10^{-5}\ m^3/s]$
Basic simulation	4.49	3.14	4.07	2.32

internal wall in the riser. Consequently, the liquid velocity is also higher in the wall region than in the center of the riser. This affects the gas separation at the top. So, more gas can be dragged into the downcomer. This is described with the carry-under model, which is shown in appendix E.

The liquid velocity in the riser is higher in the wall region than in the center of the riser, when the gas inlet is next to the wall (j=4) and also when a water channel is next to the internal wall (j=2). The liquid velocities are nearly the same in the x-direction of the riser when the gas inlet is near the internal wall. While the liquid velocity changes in the x-direction when the water channel is next to the internal wall. It can also be seen that the liquid velocity is the lowest at the place where the gas hold-up is the lowest. This is logical as the liquid flow is induced by the presence of the bubbles. The higher the gas fraction, the higher the driving density difference, the higher the driving force of gravity. When the grid cells are doubled maybe this velocity field is not found, because refining of the grid gives in general

more accurate solutions.
It can also be said that the liquid velocities in the riser and downcomer are depending on the distance from the front and back wall, coming to the wall the wall friction increases. This can be seen in figure 5.3. Furthermore, the gas inlet is not at the

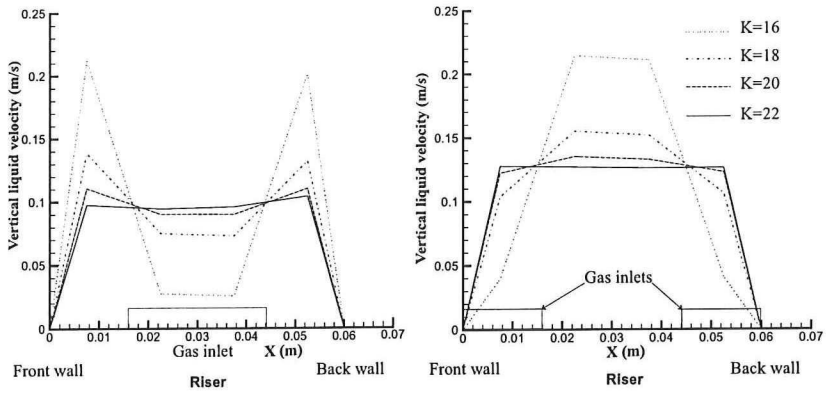

Figure 5.3: Liquid velocity for different k-planes at (a) i=12 and (b) i=13

same position in the different j-planes. The gas inlet is next to the wall in the first j-plane picture of figure 5.1 and the water channel is next to the internal wall in the other j-plane picture. So, there is a difference between the both i-planes of figure 5.3 at the k-planes near the gas inlet. The k-planes just above the gas inlet gives a high liquid velocity above the water channel. It decreased at this position and increased above the gas inlet when we goed higher in the riser. The liquid velocity is nearly constant when the k-plane is high enough above the gas inlet (k=22). The liquid velocity is much lower at the region next the walls and is zero at the walls.
The liquid velocity at k=22, j=12 is a little lower than the liquid velocity at k=22, j=13. This can be explain by the fact that the i=12 plane is near to the internal wall and i=13 is more to the center of the riser. The difference in inlet geometry will be further discussed in section 5.4.

$U_{liq,r}^{sup}$ and $U_{gas,r}^{sup}$ are 0.114 m/s and 0.65 cm/s, respectively. The superficial gas velocity is not the same as the superficial inlet gas velocity of the riser, because gas circulate through the airlift which result in a higher gas flow. With the mean gas fraction in the riser, $\alpha_r = 0.0449$, the gas and liquid velocity can be calculated, because:

$$U_{liq,r}^{sup} \simeq (1- < \alpha_{gas,r} >)U_{liq} \tag{5.1}$$

$$U_{gas,r}^{sup} \simeq < \alpha_{gas,r} > U_{gas} \tag{5.2}$$

So, the U_{liq} and U_{gas} are 0.119 m/s and 0.144 m/s, respectively. The gas and liquid velocity results in a slip velocity of 2.5 cm/s, namely:

$$U_{gas} \simeq U_{liq} + v_{slip} \tag{5.3}$$

The calculated slip velocity is around 10 times lower than the value given in literature, [Mudde and Simonin, 1999], and can not be true. The gas bubbles are more slowed down by the liquid in the basic simulation in contrast with the literature. Consequently, the mean gas fraction in the riser will be higher. The gas bubbles can not really escape from the liquid flow, because the slip velocity is very low. So, more gas enters the downcomer which results in a high gas hold-up in the downcomer.

In the basic case the outlet type II is used, so there is not a true free surface. The total volume of the mixture phase is fixed in the total domain and is therefore not a realistic scenario. For this reason other types of outlet are tested.

5.2 Influence of time step

In the first place the time step dependence of the base-setup will be investigated. Therefore, all attributes are the same as the basic simulation, except for the time step, which is varied from $1 \cdot 10^{-4}s$ to $1 \cdot 10^{-2}s$ in a logaritmisch way. Simulations with time step smaller than $1 \cdot 10^{-4}s$ are not presented, because these simulations give a rapid divergence detection and are aborted.
The flow fields and gas hold-up are shown in figure 5.2 with the time step $1 \cdot 10^{-2}s$ and $1 \cdot 10^{-3}s$. The flows and gas hold-up of the simulations at a time step of $1 \cdot 10^{-4}s$

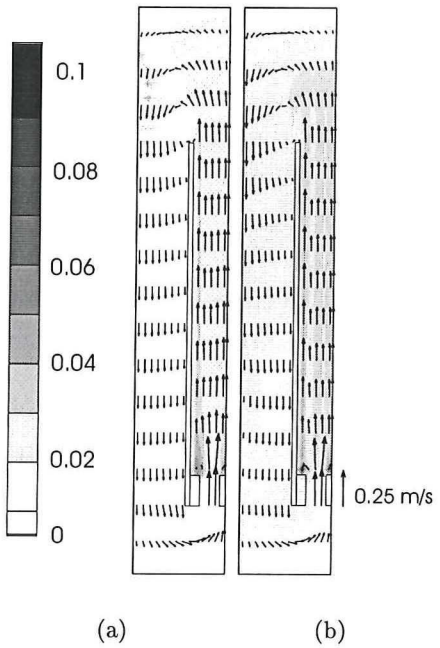

Figure 5.4: Gas hold-up distribution and liquid velocity field simulated with a time steps of (a) $1 \cdot 10^{-2}s$ and (b) $1 \cdot 10^{-3}s$ both at j=3

are not shown, but are nearly the same as the results with a time step of $1 \cdot 10^{-3}s$.

Comparing the simulations with time step $1 \cdot 10^{-2}s$ and $1 \cdot 10^{-3}s$ the gas hold-up in the downcomer is much higher in the second case. In the first case there is nearly no gas dragged into the downcomer. This difference can be explain by the flow field and gas hold-up in the riser.
The slip velocity of the simulations with time step of $1 \cdot 10^{-3}s$ is already calculated, namely $v_{slip} = 2.5cm/s$. For the simualtions with time step of $1 \cdot 10^{-2}s$ the slip velocity is 14.3 cm/s, because the superficial gas and liquid velocity in the riser are 0.45 cm/s and 0.161 m/s, respecitively, which results in a gas and liquid velocity of 0.31 m/s and 0.163 m/s, respectively. The slip velocity of simulations with time step $1 \cdot 10^{-2}s$ is more in agreement with literature than the slip velocity at time step $1 \cdot 10^{-3}s$. Therefore, the gas hold-up in the downcomer is much lower in the simulations with time step of $1 \cdot 10^{-2}s$.
Furthermore, the gas flow out of the gas inlet near the internal wall is not splitted in two straight line when the time step is $1 \cdot 10^{-2}s$ in contrast with the results at time step $1 \cdot 10^{-3}s$. And the total gas distribution of simulation with a time step of $1 \cdot 10^{-2}s$ looks more like simulations by [Mudde and Akker, 2001] than the simulations with a time step of $1 \cdot 10^{-3}s$.
The difference between these simulations is very strange, because normally the more realistic results are found when the time step is the lowest. But from the results of the present cases, it is found that the results of simulations with the highest time step are closed to reality. This may be explained by the virtual mass interaction force, because this force is depending on the acceleration which included the inverse of the time step. This is described in the next subsection.

5.2.1 Virtual mass

The virtual mass is an interaction forces for two-phase flow (see section 3.1.2), which is depending on the acceleration of the gas and the liquid phase. This acceleration includes the inverse of the time step two times. Fluent is not explicit about the discretisation of this force. It is possible that in the calculation of the virtual mass the acceleration part is calculated in the following way:

$$\alpha \rho_{liq} C_{vm} \left(\frac{\Delta U_{gas}}{\Delta t} - \frac{\Delta U_{liq}}{\Delta t} \right) \tag{5.4}$$

In this way the inverse of Δt is present. For trancient simulations the virtual mass force is integrated over a small time interval (see equation 3.50 in section 3.3.4), therefore Δt canceled out. When Δt decreases, ΔU also decreased but not necessarily with the same steps and can therefore not be controlled with the time step. With a higher virtual mass force the gas bubbles are slowed down, the accelerating of the bubble decreases, and the gas hold-up in the riser and downcomer increases as consequence. As a result, the liquid velocity might decrease in the riser and in the downcomer.

In figure 5.5 results of simulations without virtual mass are shown for different

time steps. When the virtual mass is not taken into account all calculations with time step smaller than $1 \cdot 10^{-2}s$ have nearly the same flow field, and look like the simulations with virtual mass at a time step of $1 \cdot 10^{-2}s$ i.e., no gas is dragged into the downcomer. But the riser and downcomer gas fraction and the liquid flow are lower and the gas velocities is higher in the simulations without virtual mass, as shown in table 5.2. When the virtual mass is neglected, lesser liquid is associated

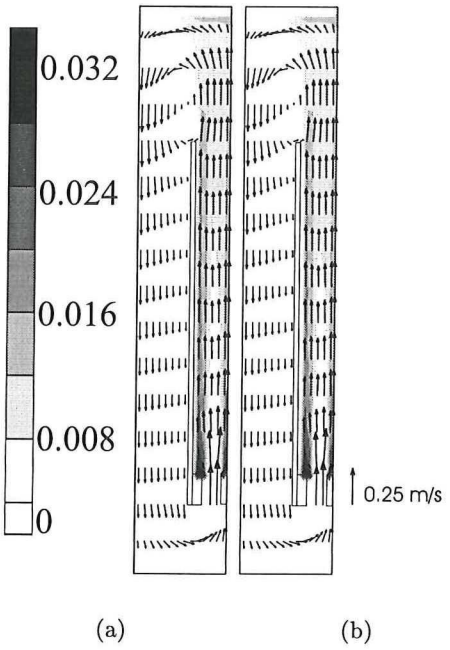

Figure 5.5: Gas hold-up distribution and liquid velocity field of simulations without virtual mass for different time step at j=3 (a) $1 \cdot 10^{-2}s$ (b) $1 \cdot 10^{-3}s$

Table 5.2: Gas hold-up in the riser and downcomer and the liquid and gas flow for simulations with and without virtual mass for different time step

	$\langle \alpha_r \rangle$ [%]	$\langle \alpha_d \rangle$ [%]	ϕ_{liq} $[\cdot 10^{-4} m^3/s]$	ϕ_{gas} $[\cdot 10^{-5} m^3/s]$
Virtual mass; time step $1 \cdot 10^{-2}s$	1.47	0	5.76	1.61
Virtual mass; time step $1 \cdot 10^{-3}s$	4.49	3.14	4.07	1.61
No virtual mass; time step $1 \cdot 10^{-2}s$	1.03	0	5.00	1.61
No virtual mass; time step $1 \cdot 10^{-3}s$	1.03	0	4.91	2.32

with the gas bubbles so, the mass of the bubbles seems lower. The gas fraction is also decreased, because the gas velocity is higher. The slip velocities, which is calculated with the superficial liquid and gas velocities and gas hold-up, is nearly the same for the different time step simulations without virtual mass, namely 0.30 m/s. Therefore, the great difference in the slip velocity of the simulations with virtual mass is totally caused by the virtual mass. The slip velocity in the simulations

without virtual mass is really high, because the virtual mass, which decreases the gas velocity and increases the liquid velocity, is neglected.
The virtual mass has to be taken into account in the simulations of the airlift loop reactor, but not in the form of equation 3.15. Perhaps, the expression of Simonin for virtual mass, with the drift velocity, can better be used.

5.3 Influence of gas inlet fraction

The influence of the gas inlet fraction on the liquid velocity and the gas hold-up in the riser and downcomer are illustrate in this section. The gas inlet fractions are varied from 1.2% to 10% which results in a superficial inlet gas velocity of 0.15 cm/s to 1.25 cm/s. Higher gas inlet fraction leads to results which are not converged. Only the gas inlet fractions and the time step are different from the basic simulation. In this section the simulations are described for time steps of $1 \cdot 10^{-2}$ and $1 \cdot 10^{-3}s$. Figure 5.6 and 5.7 depict the gas hold-up pattern and the liquid velocity field of the airlift loop reactor at a time step of $1 \cdot 10^{-2}$ and $1 \cdot 10^{-3}s$, respectively. The

Table 5.3: Superficial gas velocities for all gas inlet fraction with no circualation of the gas phase

Gas inlet fraction [%]	$U_{gas_{in}}^{sup}$ $[cm/s]$
1.2	0.15
2.4	0.30
3.6	0.45
5.0	0.65
7.5	0.94
10.0	1.25

difference between the simulations with different time step is already discussed in section 5.2, the present section focuses on the difference between the different gas inlet fractions. Figure 5.6 shows clearly that the gas hold-up and the liquid velocity increase with higher gas inlet fraction in the riser. Furthermore, the gas enters more and more into the downcomer with an increase in the gas inlet fraction. It begins to enter the downcomer when the gas inlet fraction is 5% ($U_{gas_{in}}^{sup} = 0.65cm/s$). These results meet to expectations. Namely, when the gas inlet fraction increases, the liquid velocity in the riser and downcomer increases too. Therefore, more bubbles can be dragged with the liquid into the downcomer.

The gas hold-up in the riser and downcomer increases also at higher gas inlet fraction with a time step of $1 \cdot 10^{-3}s$, as can be seen in figure 5.7. The gas enters the downcomer already at a gas inlet fraction of 1.2% ($U_{gas_{in}}^{sup} = 0.15\ cm/s$) and circulates also at this gas inlet fraction. It can not be seen in the figure, but the gas fraction in the below part of the downcomer is around 1 %. Also, the liquid velocity increases, but the liquid flow field for a gas inlet fraction greater than 5% ($U_{gas_{in}}^{sup} = 0.65\ cm/s$) is very chaotic in the riser. The only explanation which can be found for this chaotic

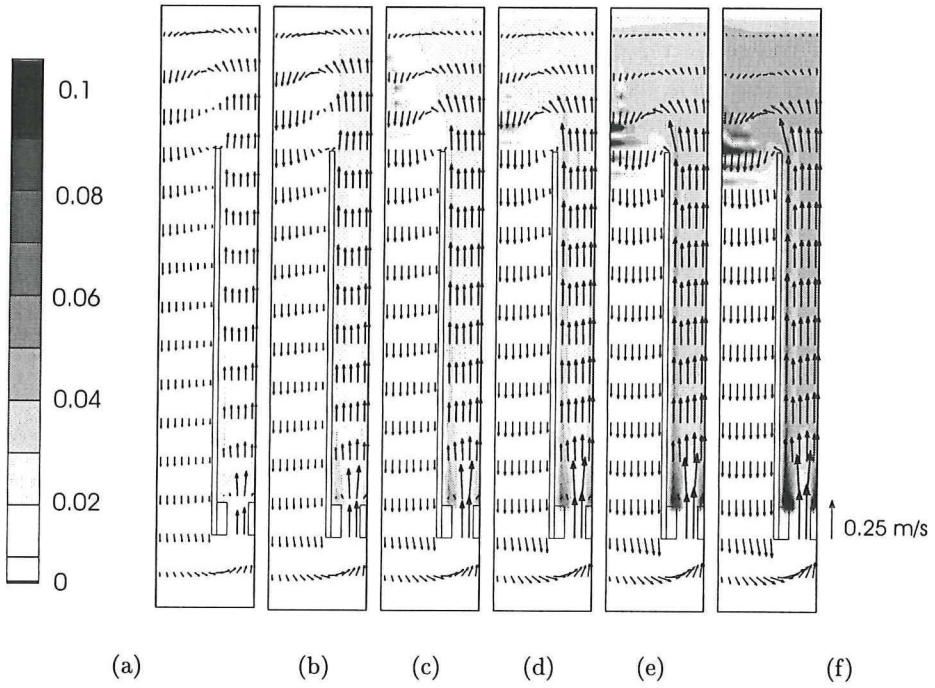

Figure 5.6: Gas hold-up distribution and liquid velocity field at t=160 s with difference gas inlet fraction (see figure), resulting in different superficial inlet gas velocity for a time step of $1 \cdot 10^{-2}s$ *at j=3 (a)* $U^{sup}_{gas_{in}} = 0.15cm/s$ *(b)* $U^{sup}_{gas_{in}} = 0.30cm/s$ *(c)* $U^{sup}_{gas_{in}} = 0.45cm/s$ *(d)* $U^{sup}_{gas_{in}} = 0.65cm/s$ *(e)* $U^{sup}_{gas_{in}} = 0.94cm/s$ *(f)* $U^{sup}_{gas_{in}} = 1.25cm/s$

flow is the high gas hold-up. Maybe simulations in fluent with time step smaller than $1 \cdot 10^{-2}$ can not really be done with high gas hold-up.
Another striking point is the splitted gas flow just above the gas inlet at the internal wall, which is discussed in section 5.1.2. This splitting is only present when the gas inlet fraction is greater or equal 3.6% ($U^{sup}_{gas_{in}} = 0.45\ cm/s$) and at really high gas fraction (higher than 5% ($U^{sup}_{gas_{in}} = 0.65\ cm/s$)) the splitting is between the gas inlets. Maybe the splitting of the gas can be explained partly by the circulation of the gas. Namely, gas enters the riser at the bottom of the riser and flows, together with the liquid, between both gas inlets. So, extra gas is concentrated at these locations and therefore, the gas flow looks splitted in the riser. Obviously, the lateral mixing of the gas is insufficient to smooth the gas fraction.

5.3.1 Comparison simulations and mechanical energy balance

A one dimensional model for the two-phase flow in an airlift loop reactor, the mechanical energy balance (see section 2.5), is used to calculate the liquid circulation velocity and the gas hold-up and in this section they are compared with the simulation results. In the calculations of the mechanical energy balance the gas hold-up in

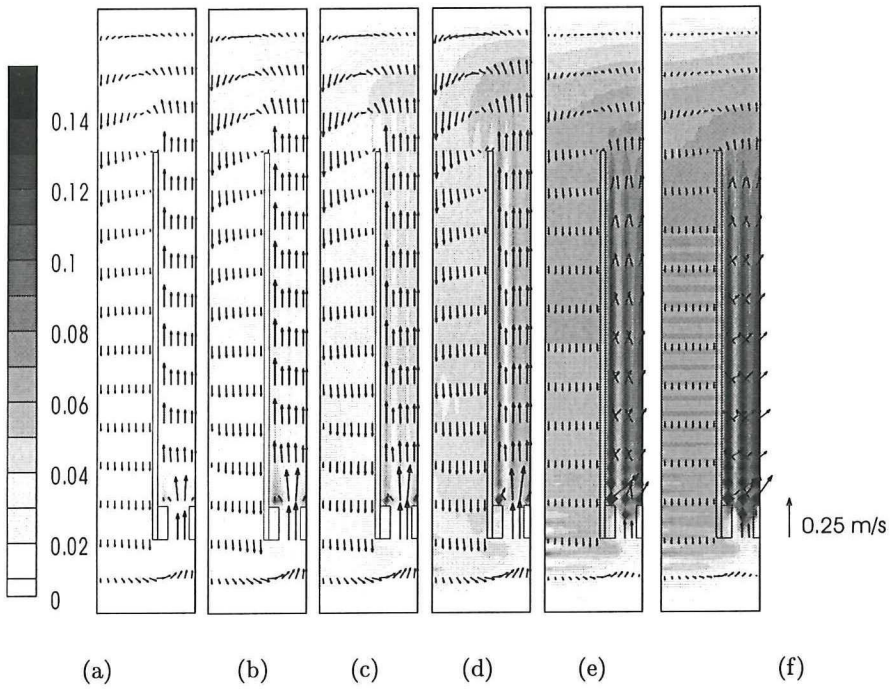

Figure 5.7: Gas hold-up distribution and liquid velocity field at t=160 s with difference gas inlet fraction (see figure), resulting in different superficial inlet gas velocity for a time step of $1 \cdot 10^{-3}s$ *at j=3 (a)* $U^{sup}_{gas_{in}} = 0.15cm/s$ *(b)* $U^{sup}_{gas_{in}} = 0.30cm/s$ *(c)* $U^{sup}_{gas_{in}} = 0.45cm/s$ *(d)* $U^{sup}_{gas_{in}} = 0.65cm/s$ *(e)* $U^{sup}_{gas_{in}} = 0.94cm/s$ *(f)* $U^{sup}_{gas_{in}} = 1.25cm/s$

the downcomer is defined zero, $\alpha_D \equiv 0$. Furthermore, the friction loss factor, which is present in the airlift loop reactor, is estimated in appendix A and is taken to be $K_f = 4.3$.

The simulated values for the gas hold-up and the superficial liquid velocity can not be compared directly to the values from the mechanical energy balance, because the gas hold-up in the downcomer is not zero in the simulations, with the exception of the simulations with low gas inlet fraction ($< 3.6\%$, $U^{sup}_{gas_{in}} = 0.45cm/s$) at a time step of $1 \cdot 10^{-2}s$. Therefore, the friction loss factor is calculated with the help of the results of these last simulations, to check the estimated value of appendix A. From these simulations the value for the friction loss factor has to be 7.8, and is higher in contrast to the estimated value of 4.3. The estimated value gives a good approximation, but is not totally correct, so a little change is surely possible. However, the difference between both values is rather high. Partly it can explain by the gas hold-up, namely, the individual plumes penetrate further into the riser in the simulations and one-dimensional calculations assume the riser gas hold-up uniform. Furthermore, there is maybe an extra friction loss in the simulated airlift, which is not taken into account.

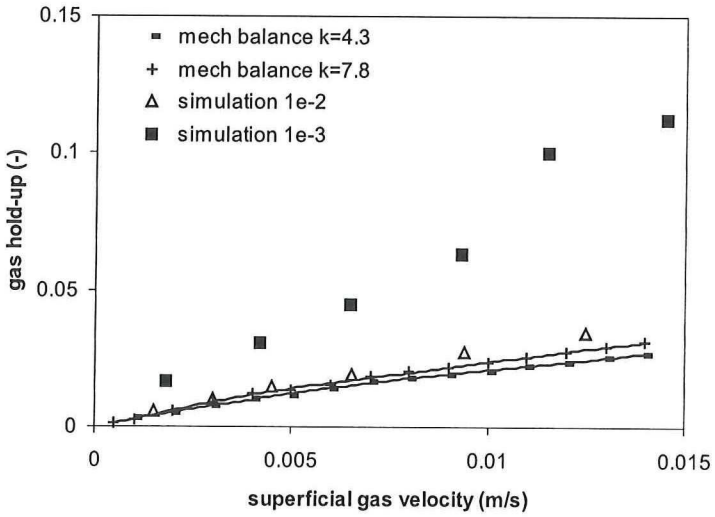

(a)

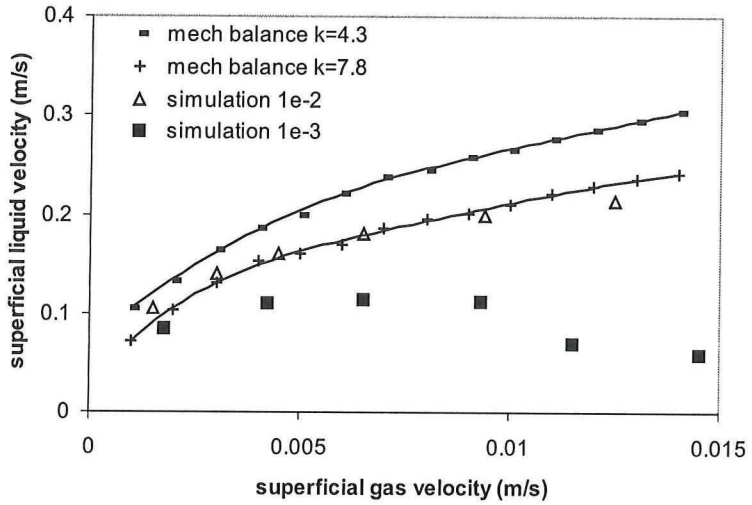

(b)

Figure 5.8: Comparison of mechanical energy balance and CFD simulations for various gas flow rates with a time step of $1 \cdot 10^{-2}s$ and $1 \cdot 10^{-3}s$ (a) gas hold-up versus superficial gas velocity (b) liquid velocity versus superficial gas velocity

The mean gas fraction and superficial liquid velocity are shown in figure 5.8 for the estimated and calculated value of K_f, together with the simulation values for a time step of $1 \cdot 10^{-2}s$ and $1 \cdot 10^{-3}s$. The liquid velocity of the simulations and the one dimensional values have a similar shape, just as the gas hold-up. But both simulations have a lower superficial liquid velocity in comparison with the values obtained from the mechanical energy balance with $K_f = 4.3$.
The values agree the best with the simulations with a time step of $1 \cdot 10^{-2}s$. The superficial liquid velocity results of the simulation with time step of $1 \cdot 10^{-2}s$ are in good agreement with the calculations with a friction factor of 7.8. The values of the other simulations (time step of $1 \cdot 10^{-3}s$) are much lower and behave very strange. The mean gas hold-up in the riser is higher in the simulations with time step of $1 \cdot 10^{-3}s$ compared to the values obtained from the mechanical energy balance with $K_f = 4.3$ or $K_f = 7.8$. The mean gas hold-up of the simulations with time step $1 \cdot 10^{-2}s$ are nearly the same as the values obtained from the mechanical energy balance with both friction loss factors. When the superficial gas velocity increases the gas hold-up increases more when the friction loss factor is higher. Therefore, the results from the mechanical energy balance using a friction loss factor of $K_f = 7.8$ are in better agreement with the simulated results.
The constraint for the mechanical energy balance, $\alpha_D \equiv 0$, is not always fulfilled in the simulations i.e., when the superficial gas velocity is higher than 0.45 cm/s gas is dragged into the downcomer. The mean gas fraction increases faster and the superficial liquid velocity increases slower at higher superficial gas velocity of the simulations with time step $1 \cdot 10^{-2}s$ in contrast to the mechanical energy balance with $K_f = 7.8$. So, the mean gas fraction and the superficial liquid velocity changes, first increases faster and the second increases slower, when the gas is dragged into the downcomer. The increase in the mean gas hold-up is caused by the gas, which is present in the downcomer, because the gas which is flowing through the downcomer enters the riser together with the gas inlet fraction.

5.4 Different inlet geometries

The simulations, which are discussed in this section, are used to assess the influence of the inlet geometry on the water velocity and the gas hold-up in the riser and downcomer. The different kind of inlets, which are used, are partly shown in figure 5.9 namely, channel at wall, sparger between wall and center, sparger at wall and a kind of checkerboard.
The surface area of the gas inlet is different from the surface area in the basic simulation (checkerboard sparger). Therefore, the superfial inlet gas velocity is different at a given gas inlet fraction, and with different circulation in the airlift. The superficial gas velocities are $U_{gas_{in}}^{sup} = 0.45cm/s$ and $U_{gas_{in}}^{sup} = 0.36cm/s$ for the basic simulation (checkerboard sparger) and the other simulations, respectively. All the other attributes are the same as in the basic simulation.

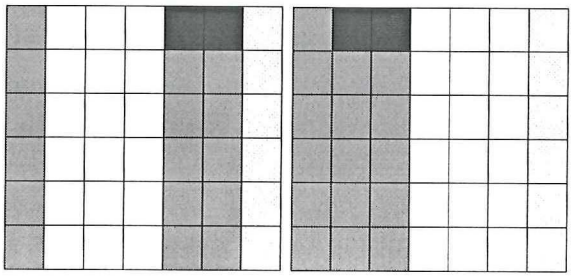

(a) channel at wall (b) sparger at wall

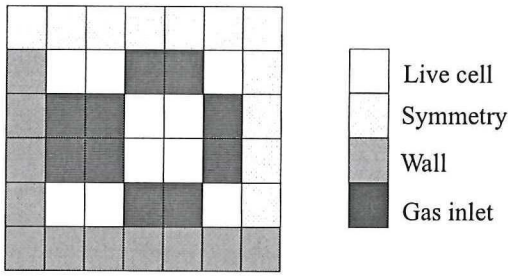

(c) checkerboard sparger

Figure 5.9: Difference inlet geometries (a) side view of channel at wall (b) side view of sparger at wall (c) top view of checkerboard sparger

Figure 5.10 and 5.11 depict the gas hold-up distribution and the liquid flow respectively, in the airlift loop reactor for the difference gas inlet geometries. From the figures it is clear that a relatively small change in the inlet geometry has serious consequences for the gas distribution and the liquid velocity. The gas distribution in the riser is more even in the case when a channel is present at the wall in the riser part. When the sparger is against the wall the gas flow is splitted in two straight lines, one against the internal wall and one a quarter of the total riser from the internal wall, see also the discussion of the basic simulation in section 5.1.2. When the sparger is in the center of the riser the gas distribution is the best namely, the gas distribution is the most even in the riser, which is necessary for the good contacting of the gas and the liquid phase. It is even better than the checkerboard configuration, for which the best gas distribution in the riser was expected, because the gas is already divided over the cross section. When we look at the results of the simulation with the sparger next to the internal wall (d) the gas hold-up can not be in a stationair situation. But all results which are shown have the same simulation time and Fluent gives a 'steady-state' time dependent result for all simulation namely, the simulation is converged with minimal residual sum of $1 \cdot 10^{-3}$ in one simulation for each time step. This criterion is therefore not always right, see for discussion the beginning of chapter 5.

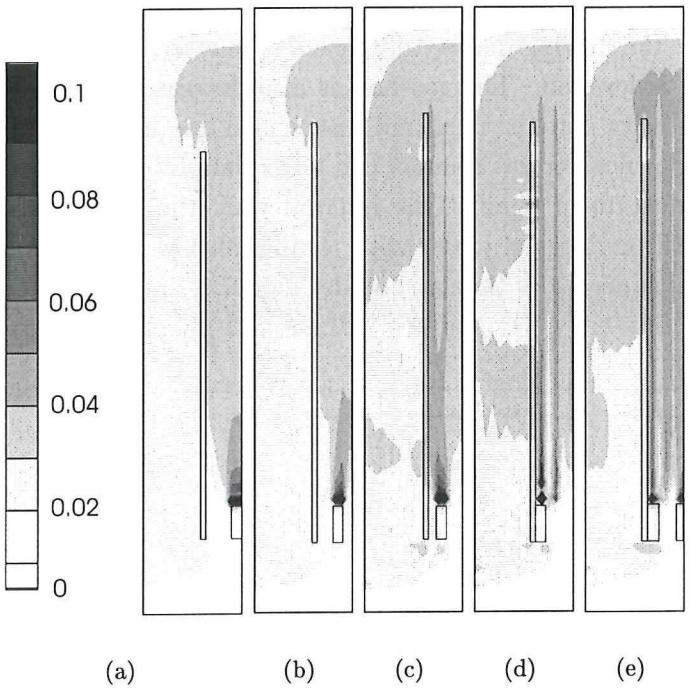

Figure 5.10: Gas hold-up distribution for difference geometry of the gas inlet (a) sparger in center (b) sparger closest center (c) sparger closest internal wall (d) sparger at internal wall (e) kind of checkerboard sparger all at j=3

In table 5.4 the mean riser and downcomer gas fraction are shown for the difference inlet geometries. The difference in the gas hold-up between the checkerboard sparger

Table 5.4: Gas hold-up in the riser and downcomer and the liquid and gas flow for difference inlet geometry

Inlet geometry	$\langle\alpha_r\rangle$ [%]	$\langle\alpha_d\rangle$ [%]	ϕ_{liq} $[\cdot 10^{-4} m^3/s]$	ϕ_{gas} $[\cdot 10^{-5} m^3/s]$
Sparger in center	3.74	2.57	4.49	2.04
Sparger closest center	3.72	2.56	4.76	2.13
Sparger closest internal wall	4.04	2.98	4.26	2.12
Sparger at internal wall	4.06	3.03	3.69	1.92
Checkerboard sparger	4.49	3.14	4.07	2.32

and the others can be explain by the size of the total inlet. Therefore, the superficial inlet gas velocities are 0.45 cm/s and 0.36 cm/s for the checkerboard sparger and the other simulations, respectively. In these simulations, without the basic simulation, the gas hold-up in the riser and downcomer increases when the sparger is closed to the internal wall. The increase of the riser gas fraction can be explain by the higher downcomer gas fraction. Namely, the gas enters the downcomer at the top

of the airlift loop reactor and the most gas leaves the downcomer at the bottom of the airlift and enters the riser. Furthermore, due to the increased gas hold-up in the downcomer, the driving density difference is reduced. Consequently, the liquid circulation rate is lowered. The gas flow is also decreased which lead to a nearly constant slip velocity and the riser and downcomer gas hold-up will increase. The increase of the downcomer gas fraction can be explain by the inlet geometry. When the sparger is next to or against the internal wall, the gas, which flows up in a straight line, will be dragged easier with the liquid flow into downcomer, see also appendix E, which describes the carry-under model.

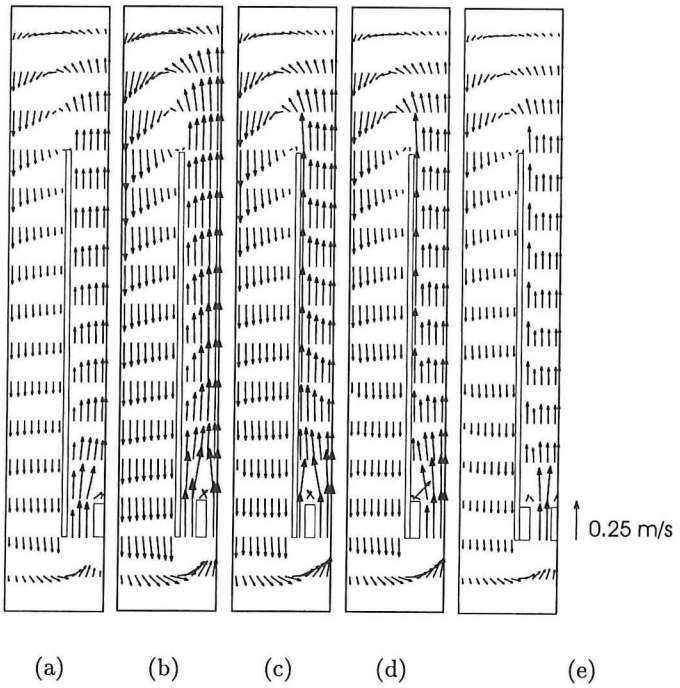

Figure 5.11: Liquid velocity flow for difference geometry of the gas inlet(a) sparger in center (b) sparger closest center (c) sparger closest internal wall (d) sparger at internal wall (e) kind of checkerboard sparger at j=3

From figure 5.11 and table 5.4 it can be seen, that the liquid flow and velocity are much higher in the airlift loop reactor when the sparger is located closest to the center of the riser. This is not true for the airlift loop reactor with the gas inlet in the center of the riser. A reason for the higher liquid flow and velocity in the riser and downcomer is that the liquid is splitted by the gas inlet at the beginning of the riser. So, the liquid enters the riser at both sides of the gas inlet and, maybe therefore, the liquid is more pulled and gives higher liquid flow in this way. Furthermore, the liquid velocity near the internal wall increases when the sparger is more and more near the internal wall. So, the liquid velocity in figure 5.11b has a lower liquid velocity as figure 5.11c. This is a consequence of the gas hold-up distribution near the internal wall. Namely, the liquid velocity is dependent on the gas hold-up, when the gas hold-up increases the local liquid velocity increases too. So, when the gas

hold-up near the internal wall is high, the local liquid velocity will also be high at that position. This is also seen in the results with sparger in the middle of the riser. Namely, the gas hold-up and the liquid flow rate are both the highest in the center of the column, above the gas inlet.
The liquid flow is decreased when the sparger is more and more near the internal wall and also the difference in gas hold-up between the riser and downcomer decreases. This is caused by the wall friction, namely, when the liquid velocity at the wall is high the wall friction increased. This higher wall friction influence the liquid circulation and the difference in gas hold-up.

5.5 Interphase turbulent momentum transfer

The interphase turbulent momentum transfer functions (equations 5.5 and 5.6) can only be calculated when there is a dilute secondary phase [Fluent Inc., 1998]. In a dilute secondary phase the gas bubbles are not close to each other, so the drift velocity can surely be used. Simulations with no-dilute secondary phase are aborted in Fluent.

$$\Pi_{k_{liq}} = \frac{K_{21}}{(1-\alpha)\rho_{liq}}(k_{12} - 2k_{liq} + (\vec{U}_{gas} - \vec{U}_{liq}) \cdot \vec{U}_d) \tag{5.5}$$

$$\Pi_{\epsilon_{liq}} = C_{3\epsilon}\frac{\epsilon_{liq}}{k_{liq}}\Pi_{k_{liq}} \tag{5.6}$$

$$\vec{U}_d = -D_{12}^t\left(\frac{1}{\sigma_{21}\alpha}\nabla\alpha - \frac{1}{\sigma_{21}(1-\alpha)}\nabla(1-\alpha)\right) \tag{5.7}$$

Probable the inverse of the liquid distribution $(1-\alpha)$, which is enclosed in the drifting velocity U_d (equation 5.7 see also section 3.1.2), is the reason. Namely, when the gas fraction increases the liquid fraction decreases at any place, because $\alpha + (1-\alpha) = 1$.

$$K_{21} = \frac{3}{4}C_D\alpha\frac{|U_{liq} - U_{gas}|}{d_{gas}^2} \tag{5.8}$$

When K_{21} (equation 5.8) is multiplied with the drift velocity the gas fractions canceled each other out, but the inverse of the liquid fraction is even present in square. Consequently, high gas fraction gives a high $\Pi_{k_{liq}}$ and $\Pi_{\epsilon_{liq}}$, which can not be true and take care of high dissipation rates. Therefore, only simulations with low gas hold-up ($\alpha < 0.6$) can be calculated in this way. The interphase turbulent momentum transfer functions are not present in the simulations without transfer function. This is the only difference in contrast with the basic simulation.

The interphase turbulent momentum transfer terms include the diffusion of the gas phase due to the turbulent flow. When these terms are neglected the diffusion in the airlift loop reactor is much smaller. Comparing this simulation with simulation with interphase turbulent momentum transfer, the basic simulation, (see also figure 5.12 and 5.13) shows that the diffusion in the I-direction and J-direction, i.e. perpendicular to the main flow direction, is really much smaller by neglecting the transfer terms. Nearly all the gas stays above the gas inlet sparger and the liquid is dragged

upwards by this gas flow. As a consequence, the liquid velocity is highest above the gas inlet sparger. The gas, liquid flow and gas distribution are more chaotic in the case when the interfacial turbulent momentum transfer is neglected. This is caused by the neglecting of the diffusion in the airlift loop reactor.
The liquid flow is shown in table 5.5. When the interphase turbulent momentum transfer terms are neglected the circulation liquid flow decreases. So, the gas bub-

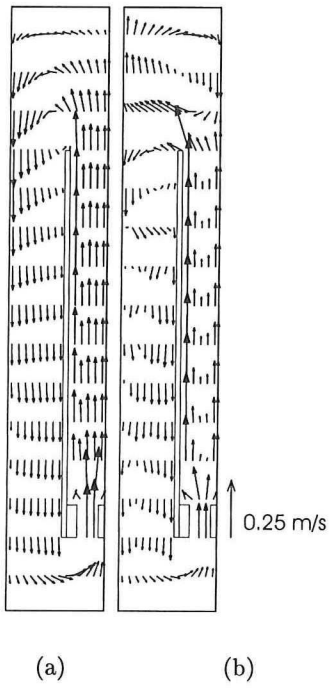

Figure 5.12: Liquid velocity flow field for simulations with and without the interfacial turbulent momentum transfer at j=3 (a) simulation with transfer function (b) simulation without transfer function

bles stay for a longer time in the airlift loop reactor. Therefore, more gas is present in the riser, which is also shown in this table. The gas hold-up in the downcomer

Table 5.5: Gas hold-up in the riser and downcomer and the liquid flow for simulations with and without interfacial turbulent momentum transfer

	$\langle\alpha_r\rangle$ [%]	$\langle\alpha_d\rangle$ [%]	ϕ_{liq} [$\cdot 10^{-4} m^3/s$]
With transfer function	4.49	3.14	4.07
Without transfer function	4.99	3.79	2.62

is also higher in the simulation without interphase turbulent momentum transfer. But, the difference between the gas hold-up in the riser and downcomer is smaller. Both phenomenon, the lower liquid circulation and lower difference in gas hold-up between riser and downcomer, are a consequence of the change in mixing (diffusion) in the airlift loop reactor by the neglecting of the interphase turbulent momentum

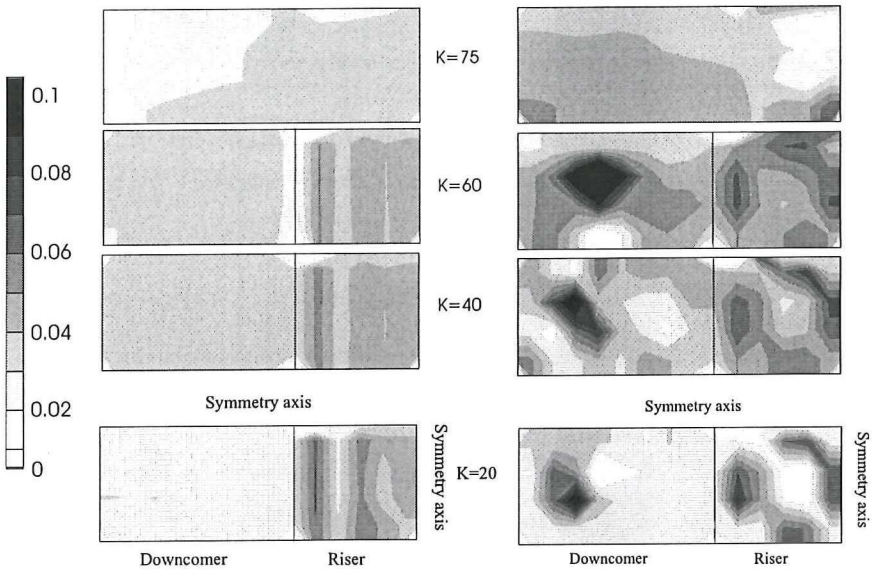

Figure 5.13: Gas hold-up distribution for simulations with and without the interfacial turbulent momentum transfer at k=20, 40, 60 and 75 (a) simulation with transfer function (b) simulation without transfer function

transfer terms.

5.6 Outlet difference

The different outlets are compared in this section. Outlet I has an outlet boundary condition which simulates a gas disengagement space patched at the top of the airlift and the outlet of type II is defined as a fixed velocity inlet, just as the basic simulation. Furthermore, the interphase turbulent momentum transfer is neglected, because the gas fraction is not dilute, which is necessary for the calculation of these transfer terms (equations 5.5 and 5.6). The simulations of outlet I are very difficult to get converged, therefore the minimal residual sum is in this case set to $2 \cdot 10^{-3}$, where the simulations of outlet I are denoted 'converged'. The other attributes are the same as in the basic simulation.

In figure 5.14 the gas hold-up distribution is shown for both kind of outlets. Just as in the simulations without interphase turbulent momentum transfer, there are gas plumes present right above the gas inlet sparger, because the turbulence diffusion is neglected. Furthermore, the gas distribution and liquid velocity are rather chaotic again, which can also be explained by the neglecting of the interphase transfer terms. A circulation of the liquid at the top of the downcomer (k=60) is present in both

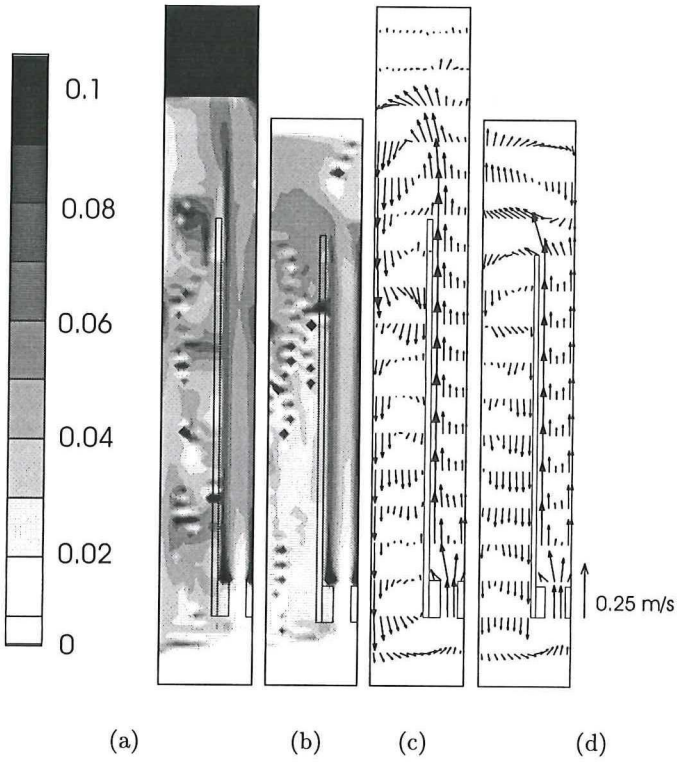

Figure 5.14: Gas fraction distribution for the simulations of (a) outlet I and (b) outlet II and liquid velocity field for simulations of (c) outlet I and (d) outlet II all without interphase turbulent momentum transfer at j=3

cases. There is a kind of circulation at the bottom of the downcomer (k=10) of the simulation with outlet I, this is shown in figure 5.14. The first circulation, at the top of the downcomer, is also found by [Mudde and Akker, 2001] and in the results of the simulation with outlet II. The second circulation is not present in the other simulations. Maybe the gas bubbles can not leave this circulation, which results in coalescence of the gas bubbles. So, this simulation is not really stationair and therefore, it is not converged with minimal residual sum of $1 \cdot 10^{-3}$.
The liquid velocity of outlet I type is lower in the center of the riser compared to the results of outlet II. Near the internal wall, however, the liquid velocity is higher for outlet I than for outlet II simulations. The liquid circulation velocity is lower and

Table 5.6: Gas hold-up in the riser and downcomer and the liquid flow for simulations with different outlets

	$\langle \alpha_r \rangle$ [%]	$\langle \alpha_d \rangle$ [%]	ϕ_{liq} [$\cdot 10^{-4} m^3/s$]
Outlet I	5.35	4.42	2.48
Outlet II	4.99	3.79	2.62
Basic simulation	4.49	3.14	4.07

the mean gas fraction in the riser and downcomer are higher for the case of outlet I. The lower liquid flow can be explained by the difference in the outlet namely, in the simulations of outlet II the gas and liquid velocities are fixed at the outlet, there is no really free surface and therefore the liquid can not flow up and down as the reality. When the fixed gas velocity at the outlet does not match with the slip velocity of the bubbles, the gas bubbles can not leave the airlift just as the reality. They are aided or hindered to leave the airlift loop reactor. Consequently, the gas and liquid velocity and therefore also the liquid flow are influenced. Furthermore, higher mean gas fractions are caused by the lower liquid velocity, because lesser liquid results in higher gas fraction in riser as well as downcomer.
Just as seen in the previous section the interphase turbulent momentum transfer terms are necessary for the simulations of the airlift loop reactor in Fluent. Therefore, only simulations of outlet type II can be done well. In this simulations the riser and downcomer gas hold-up are a little lower and the liquid flow is a little higher than simulations with outlet I.

5.7 Influence of the symmetry

The airlift loop reactor is simulated with one symmetry axis, only the vertical plane through the riser is taken as symmetry axis. So, one half of the airlift is simulated. The second symmetry axis, the vertical between the front and back wall through the riser and both downcomers, is ommited and will be denoted as 'the second symmetry axis' in what follows. The geometry of the gas inlet is a kind of checkerboard, double that which is described in section 4.2.2, therefore the gas flow is also two times and will be $3.22{\cdot}10^{-5}\ m^3s^{-1}$, but the superficial gas velocity is obviously the same, namely $U^{sup}_{gas_{in}} = 0.45\ cm/s$. All the other attributes are the same as in the basic simulation.

The gas distribution of the simulation with one symmetry axis is shown in figure 5.15 for different heights in the airlift. The gas hold-up and gas distribution in the riser and downcomer are nearly the same as those of the basic simulation. The only difference in this distribution is near the second symmetry axis. The gas hold-up near the second symmetry axis in the basic simulation is very low in contrast with the gas hold-up in the middle of the riser from the simulation without of the symmetry. This lower gas hold-up is also shown in the results of the simulation with one symmetry axis, but in this case it is present near the back wall. This lower gas hold-up is caused by the program tecplot, which sets the center cell values on the boundary of the cell. So, the values have to be transfered one half cell to the back wall. The symmetry axis is seen in the picture when the values are transfered to the back wall.
The velocity flow field does nearly not change in the j-direction of the simulations with one symmetry axis. The liquid velocity field seems nearly the same for both simulations at j=3. The total liquid flow and the averaged gas hold-up of the riser and downcomer are written in table 5.7. The total liquid flow is two times the liquid

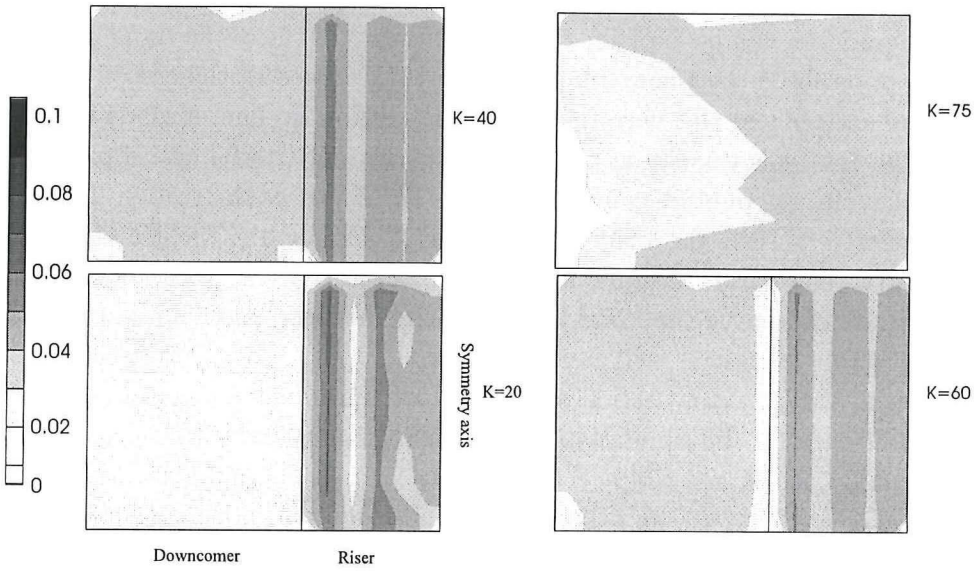

Figure 5.15: Gas fraction distribution simulated with one symmetry at k = 20, 40, 60 and 75

flow of the basic simulation. This is obviously caused by the doubling of the riser surface. The gas hold-up in the riser and downcomer are nearly the same as those of the basic simulation. From the results of this section it can be concluded that

Table 5.7: Gas hold-up in the riser and downcomer and the liquid flow for simulations with one and two symmetry axis (basic simulation).

	$\langle\alpha_r\rangle$ [%]	$\langle\alpha_d\rangle$ [%]	ϕ_{liq} [$\cdot 10^{-4} m^3/s$]
One symmetry axis	4.45	3.11	8.11
Basic simulation	4.49	3.14	4.07

the simulation with or without second symmetry axis have nearly the same results. Simulations with second symmetry axis are surely commended, because there are more grid points in the simulation without second symmetry and therefore the total simulation time is much larger.

5.8 Double grid

One simulation is done with doubled grid to show the influence of the grid in the simulations of the airlift loop reactor. So, the grid in the i and j-direction are doubled. Therefore, this grid has 30 x 10 x 80 (width x depth x height) grid cells. The grid is not doubled in the z-direction, because in this direction the results of the basic simulation are not strange, just as in the i and j-direction. All the other attributes are the same as in the basic simulation.

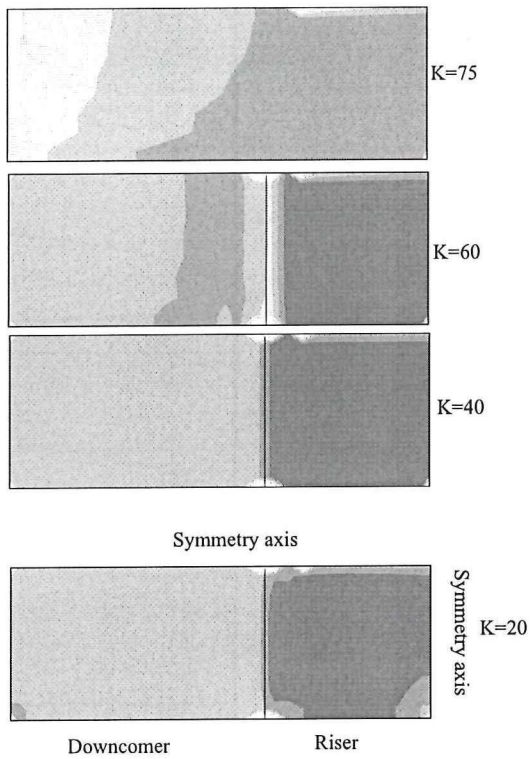

Figure 5.16: Gas hold-up distribution for simulations with redoubled grid in the I and J-direction at k=20, 40, 60 and 75

In figure 5.16 the gas hold-up distribution of the simulation with doubled grid is shown for different k-planes. The gas distribution is more equal in the riser in this simulation in contrast with the basic simulation. This can also be seen in figure 5.17 in which the gas hold-up is plotted against the position in the x-direction of the riser. This kind of gas hold-up distribution is also seen by [Mudde and Akker, 2001]. In the last figure a smaller gas hold-up is seen near the internal wall at k=60. The gas hold-up at the wall is zero and close to the wall the gas hold-up is much lower in contrast with the other planes. This can be explained by the fact that at this height the internal wall is stopped, here is a kind of liquid circulation cell present. Furthermore, the gas flow out of the sparger near the internal wall in not splitted in two straight lines, which is found in the basic simulation. Doubling of the grid in i and j-direction takes care of a better gas hold-up distribution in the riser that becomes comparable with results found in literature.
The gas hold-up at the top of the downcomer (k=60) is the greatest at the internal wall. Most of the gas at that position does not enters the downcomer, but leaves the reactor at the top of the airlift loop reactor. This can be seen in figure 5.18 were the gas hold-up distribution and the liquid flow are shown for simulations with doubled grid.

The liquid velocity flow is for all j-planes nearly the same. The liquid flow just above the gas inlet is the highest near the symmetry axis and further in the riser at the

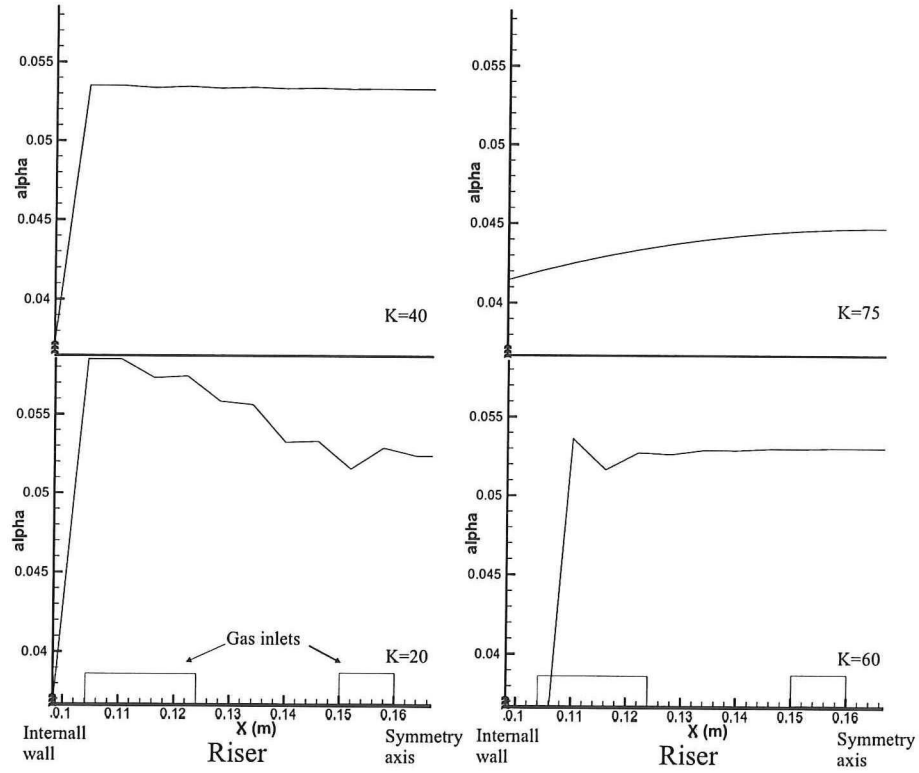

Figure 5.17: Gas hold-up distribution plotted against the position in the x-direction of the riser at different height of the airlift loop reactor at j=5

internal wall. In the downcomer this velocity field can also be seen. Because the liquid velocity at the top of the downcomer is the highest near the wall, liquid enters the downcomer. Further in the downcomer the liquid velocity is the highest near the internal wall. Doubling of the grid results in more constant liquid flow field in the riser.

Table 5.8: Gas hold-up in the riser and downcomer and the liquid flow for the basic simulation and simulation with doubled grid

	$\langle\alpha_r\rangle$ [%]	$\langle\alpha_d\rangle$ [%]	ϕ_{liq} [$\cdot 10^{-4} m^3/s$]	ϕ_{gas} [$\cdot 10^{-5} m^3/s$]
Basic simulation	4.49	3.14	4.07	2.32
Doubled grid	5.35	3.72	4.53	2.92

The mean gas hold-up of the riser and downcomer and the liquid flow are given for the basic simulation and simulation with doubled grid in table 5.8. In the simulation with doubled grid the gas hold-up in the riser and downcomer and the liquid flow are higher than in the basic simulation. But the $\Delta\alpha$ is greater in the simulations with doubled grid, so more gas leaves the reactor in a directional way through the outlet when the grid is doubled. The simulation with more grid cells give more detailed results, which give this difference.

The slip velocity of the simulation with doubled grid is nearly the same as the slip

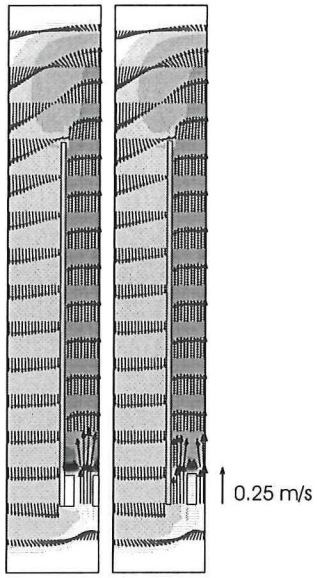

Figure 5.18: Gas hold-up distribution and liquid velocity field for simulations with doubled grid in the I and J-direction at (a) j=5 and (b) j=8

velocity of the basic simulation, namely 19 cm/s. Both flows are increased when the grid is doubled, so the gas and liquid velocities are also increased. Furthermore the gas hold-up in the riser is also increased, which results in a little lower slip velocity, because the gas hold-up increased more than the gas flow.

Chapter 6

Conclusions and Recommendations

Three dimensional simulations of rectangular airlift loop reactors have been performed by using the CFD package Fluent. For the assessment of the Euler-Euler model, Fluent has appeared to be an useful tool.
The first result presented in this thesis is that a liquid (primary phase) circulation to simulate an airlift loop reactor is an effective procedure to start the simulation of the bubbly flow in Fluent.
An very important result is that simulations with time step $\leqq 1 \cdot 10^{-3} s$ give a high gas hold-up in the downcomer and a very low slip velocity. Furthermore, they are not in agreement with predictions of the riser gas fraction and liquid circulation from an one-dimensional mechanical energy balance. However, simulations with time step $1 \cdot 10^{-2} s$ show a reasonable to good agreement with the one-dimensional mechanical energy balance. The simulations with time step $1 \cdot 10^{-3} s$ do improve substantially better when the virtual mass force is neglected, namely, the influence of the virtual mass is very high in this simulation. Results of simulations without virtual mass are nearly the same for both time steps. Probably, the virtual mass force is calculated with a dependence of ΔU (i.e., the difference in velocity between two consecutive timesteps) and an independence of Δt. So, when Δt decreases, ΔU also decreased but not necessary with the same rate and can not be controlled sufficiently with Δt. Nevertheless, the virtual mass has to be taken into account, because the slip velocity of simulations without virtual mass is really high.
The interfacial turbulent momentum transfer terms take care of diffusion and require a dilute secondary phase (gas phase). These terms can not be neglected. Consequently, simulations with outlet type I (outlet approach with a gas disengagement zone patched at the top) are not possible, because here the gas fraction is not dilute. Outlet II, outlet with fixed velocities at the top, works reasonable well but misses the flexibility to adapt to local dynamic gas throughput and velocities. The gas hold-up and the liquid flow are a little different in simulations with this outlet in comparison to simulations with outlet type I. Experimental values are needed to

compare these values with reality.
Simulation with two symmetry axis, one vertical through the riser and one vertical between front and back wall gives the same results as simulation with only the first symmetry axis. Hence, simulations can be done with two symmetry axis. So, lesser grid cells are necessary, which results in a smaller calculation time.
Simulations with refined grid give more detailed results and are surely necessary for simulation with time step of $1 \cdot 10^{-3}s$.
The investigations indicate that CFD of airlift reactors can be used to model design or tune airlift reactors. For the CFD package Fluent the following can best be used:

- Liquid circulation before starting simulation
- Drag force
- Virtual mass
- Interface turbulent momentum transfer terms
- Time step $1 \cdot 10^{-2}s$
- Outlet with fixed velocities
- Grid cells at least 30 x 10 x 80
- Two symmetry axis, one vertical through riser and one vertical between front and back wall

These result in the best and most accurate results of the simulations in this thesis.

6.1 Recommendations

For further improvement, simulations with minimal residual sum $\leqq 1 \cdot 10^{-3}$ are necessary to check the important of the time step on the calculation of the virtual mass. Furthermore, the expression of Simonin for virtual mass, with the drift velocity, has to be tested. Probably this expression can better be used. Simulations with other CFD codes can be used to give a better explanation for the results with a time step of $1 \cdot 10^{-3}s$. It is important to know, how the virtual mass force is really calculated by Fluent and by other CFD codes.
A detailed comparison with experiments is needed to see whether or not the details of the flow are simulated well.
To obtain more accurate solutions, finer grids should be used: the grid should be at least 30 x 10 x 80, but doubling the number of cells once more in all directions would be preferable.

Appendix A

Determination of the overall friction loss coefficient

The friction loss factors are estimated using the standard relations for wall friction. Theoretical K_f values for internal loop reactors, derived from one phase flow theory, were difficult to derive, because no accurate estimation of the frictional losses in the 180° turns at the top and bottom of the reactor could be made. The expression used to calculate the friction coefficient of the pipe elements and the appendages is:

$$K_f = k_{fr} + \left(\frac{A_r}{A_d}\right)^2 k_{fd} + \left(\frac{A_r}{A_d}\right)^2 k_{fdr} + \left(\frac{A_r}{A_d}\right)^2 k_{frd} + k_{fs.enl.inlet} + \left(\frac{A_r}{A_d}\right)^2 k_{fs.contr.inlet} + k_{fbents} \tag{A.1}$$

In the following the different friction losses will be described.

A.1 Reactor tubes

The friction loss coefficient in lines of circular cross section was calculated according to:

$$k_{fi} = 4f_i \frac{H_i}{D_{h_i}} \tag{A.2}$$

were f_i is the friction factor of the pseudo homogeneous mixture in section i. The value of the friction factor can estimated with the Blasius equation (equation A.3) which is true for $4000 < Re < 10^5$. The Blasius equation is:

$$4f = 0.316 Re^{-1/4} \tag{A.3}$$

So, the friction factor is around $5 \cdot 10^{-3}$, because the Reynolds number is 60000.

A.2 Appendages

The sharp bents on the riser top and bottom gives a friction factor of 1.5 per bent. So, $k_{fbents} = 3.0$.
Furthermore, there is a sudden enlargement $k_{fsud.enl.}$ on the top of the riser, k_{frd} and an sudden contraction $k_{fsud.contr.}$ on the bottom of the downcomer, k_{frd}. The first one can be described as:

$$k_{fs.enl.} = \left(\frac{A_d}{A_r} - 1\right)^2 \tag{A.4}$$

and the second one:

$$k_{fs.contr} = 0.45 \cdot \left(1 - \frac{\frac{1}{2}A_r}{A_d}\right)^2 \tag{A.5}$$

where A_r is the surface of the riser, which is simulated. Finally, there is a friction loss through the gas inlet. In the gas inlet there is a sudden contraction and a sudden enlargement, so the equations A.4 and A.5 can be used with other surfaces, namely A_d has to be A_r and A_r has to be A_{in} and the half before A_r in equation A.5 is not present in the calculation of the sudden contraction at the gas inlet.

For the airlift loop reactor, which is simulated, $K_f = 4.3$, in this the friction loss factor of the wall above and under the internal wall and the in the gas inlet are neglected.

Appendix B

Finite Volume Method

The integration of the differential equations can be illustrated most easily in simple Cartesian coordinates, and is demonstrated below for a one-dimensional equation set. Consider first the one dimensional differential equations for continuity, momentum, and a scalar quantity ϕ:

$$\frac{\partial}{\partial x}(\rho u) = 0 \tag{B.1}$$

$$\frac{\partial}{\partial x}(\rho u u) = -\frac{\partial p}{\partial x} + \frac{\partial}{\partial x}\left[\mu \frac{\partial u}{\partial x}\right] + F \tag{B.2}$$

$$\frac{\partial}{\partial x}(\rho u \phi) = \frac{\partial}{\partial x}\Sigma \frac{\partial \phi}{\partial x} + S_\phi \tag{B.3}$$

Equation B.1 through B.3 can be volume integrated over a control volume employing the Divergence Theorem:

$$\int_{volume,V} \frac{\partial}{\partial x}(\rho u) dV = \int_A \rho u \cdot dA \tag{B.4}$$

Volume integration of equation B.1 on the control volume around P of figure B.1

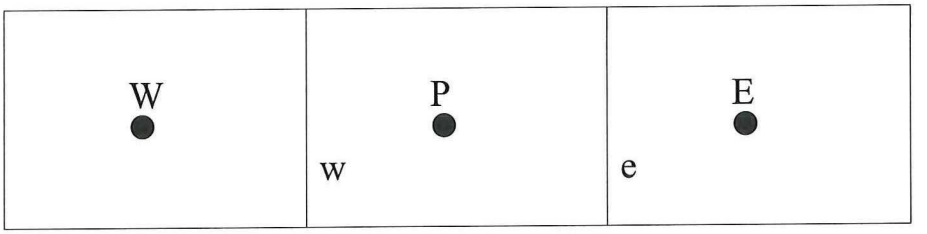

Figure B.1: One dimensional control volume nomenclature used to illustrate volume integration

thus yields:

$$(\rho u A)_e - (\rho u A)_w = 0 \tag{B.5}$$

or:

$$J_e - J_w = 0 \tag{B.6}$$

Integration of the momentum equation B.2 yields:

$$(\rho u^2 A)_e - (\rho u^2 A)_w = -(p_e - p_w)A + \left(\mu \left[\frac{u_E - u_P}{\Delta x}\right] A\right)_e - \left(\mu[\frac{u_P - u_W}{\Delta x}]A\right)_w + F\Delta V \tag{B.7}$$

or:

$$J_e u_e - J_w u_w = -(p_e - p_w)A + \left[\frac{\mu_e}{\Delta x_e}(u_E - u_P) - \frac{\mu_w}{\Delta x_w}(u_P - u_W)\right] A + F\Delta V \tag{B.8}$$

and integration of the scaler equation B.3, yields:

$$J_e \phi_e - J_w \phi_w = \left(\Sigma_e \frac{\phi_E - \phi_P}{\Delta x_e} - \Sigma_w \frac{\phi_P - \phi_W}{\Delta x_w}\right) A + S_\phi \Delta V \tag{B.9}$$

Note that the equations solved by FLUENT are extensions into three-dimensional curvilinear coordinates of those shown above for one-dimensional Cartesian coordinates.

Appendix C

Grid

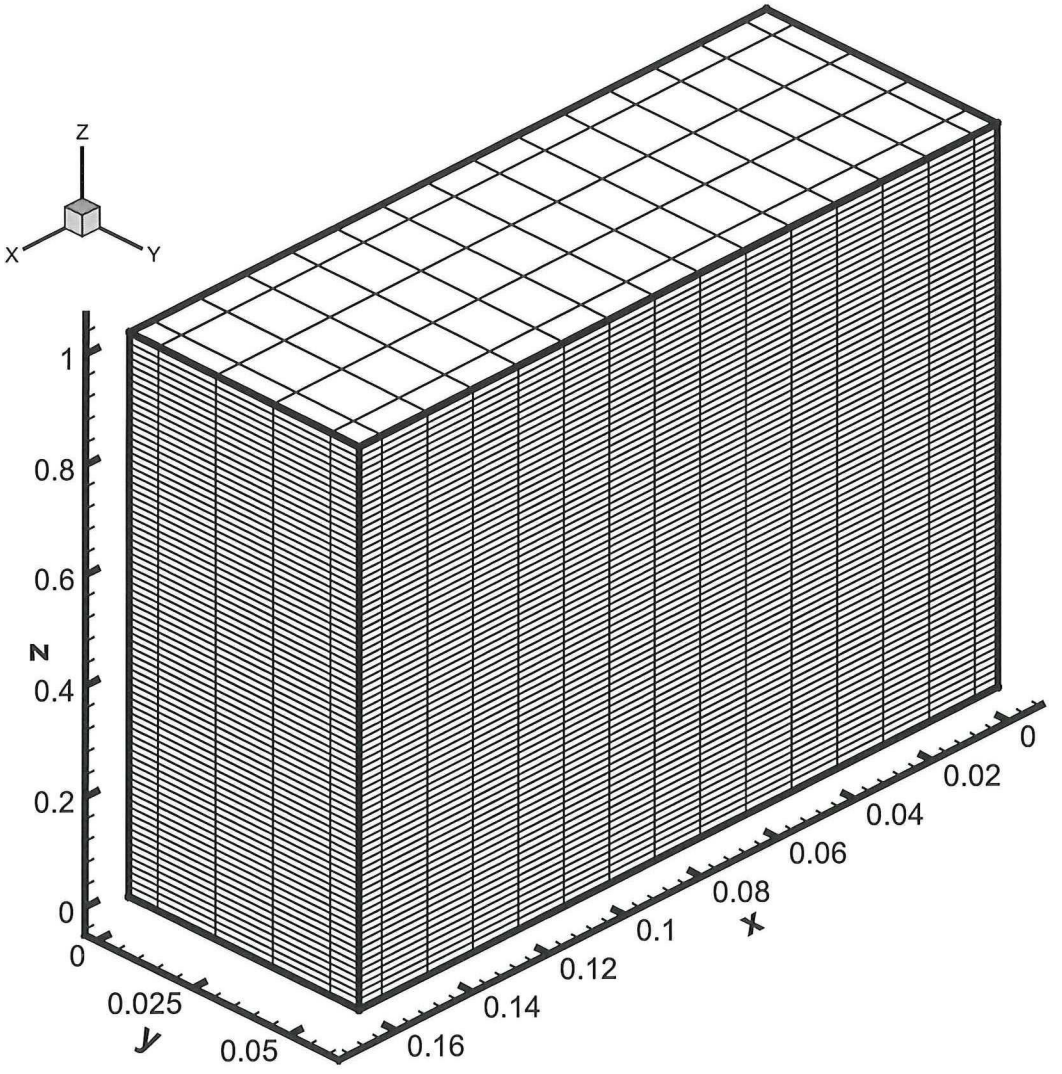

Figure C.1: Grid cell

Appendix D

Different wall functions

Two different wall functions will be described namely, the standard wall function and the two-layer-based nonequilibrium wall function.

D.1 Standard wall function

The wall boundary layer consists of a laminar sub-layer and a so-called log-law region. In the log-law region, the wall shear stress can be computed via the log-law wall function:

$$\frac{U_{p1}}{U^*} = \frac{1}{\kappa} ln(Ey^*) \tag{D.1}$$

where

$$U^* = \sqrt{\frac{\tau_w}{\rho_1}} \tag{D.2}$$

* and $_p$ indicates a point in the log-law layer and point p respectively, κ is the von-Karman's constant, E is an empirical constant set by default equal to 9.8, k_p is the turbulent kinetic energy at point p, τ_w is the shear stress at the wall and y^* is the dimensionless distance from the wall:

$$y^* = \frac{\rho_1 k_p^{\frac{1}{2}} C_\mu^{\frac{1}{4}} y_p}{\mu_1} \tag{D.3}$$

where y_p is the distance from point p to the wall.

Fluent uses an explicit approach to solution of the coupled Equations D.1 through D.3. The logarithmic law for the velocity in a turbulent flow near the wall is known to be valid for y^* >30$\sim$60. In Fluent, the log-law is employed when y^* >11.225. When y^* falls bellow this value, the near-wall center lies in the viscous sub-layer of the turbulent boundary layer. Fluent than reverts to the following equation for the shear stress:

$$\tau_w = \mu \frac{\partial u}{\partial n} = \mu \frac{\Delta u}{\Delta n} \tag{D.4}$$

since the near-wall node is in the laminar sub-layer where the wall function should not be applied. In equation D.4 u is the velocity component parallel to the wall and n is the coordinate normal to the wall. Δu and Δn are determined using values stores in the computational cell adjacent to the wall. An equilibrium assumption to derive the boundary conditions for k and ϵ is used with the standard wall function in Fluent. Under this assumption the turbulent dissipation ϵ_p is computed from:

$$\epsilon_p = \frac{C_\mu^{\frac{3}{4}} k_P^{\frac{3}{2}}}{k y_P} \tag{D.5}$$

A somewhat more general treatment of near-wall values of k and ϵ is assumed when the nonequilibrium wall function is used.

D.2 Two-Layer-Based nonequilibrium wall function

In addition to the standard wall function a two-layer-based nonequilibrium wall function is also available for turbulent flows. The two-layer wall function partly accounts for nonequilibrium effects neglected in the standard wall function. This nonequilibrium wall function can be used with the standard $k-\epsilon$ model and with the RNG $k-\epsilon$ model. The two-layer wall function employes the two-layer concept in which wall neighboring cells are assumed to consist of a viscous sub-layer and a fully turbulent layer. For the turbulence quantities the following assumptions are made:

$$\tau_t = \begin{cases} 0 & y < y_v \\ \tau_t & y > y_v \end{cases} \quad k = \begin{cases} \left(\frac{y}{y_v}\right)^2 k_p & y < y_v \\ k_p & y > y_v \end{cases} \quad \epsilon = \begin{cases} \frac{2\nu k}{y^2} & y < y_v \\ \frac{k^{\frac{3}{2}}}{C_l y} & y > y_v \end{cases} \tag{D.6}$$

where $C_l = \kappa C_\mu^{-\frac{3}{4}}$ and y_v is the dimensional thickness of the viscous sub-layer. Because of the capability to partly account for nonequilibrium effects, the nonequilibrium wall function is recommended for use in complex flows involving separation, re-attachment and impigement where the mean flow and turbulence change rapidly. Furthermore, the same limitations apply to the selection of the grid used as for the standard wall function (i.e., $y^+ > 30$ at the wall-neighboring nodes), although the nonequilibrium wall function makes the solution less sensitive to the grid used.

Appendix E

Carry-under model

The carry-under model is shown in figure E.1, in which the cross-section of the top of the riser is shown. The water above the riser and downcomer is divided into three triangular parts, which are described below:

- In the first part the gas bubbles and the liquid flow straight upwards.
- In the second part the water flows horizontally to the downcomer and the gas bubbles flows with the same horizontally velocity, because the slip velocity only has a vertical component. But the gas bubbles escape out of the liquid flow by the upward force, which works on the gas bubbles. So, the bubble flow is curved.
- In the third part the liquid flows straight downwards into the downcomer and the bubbles are dragged with the liquid.

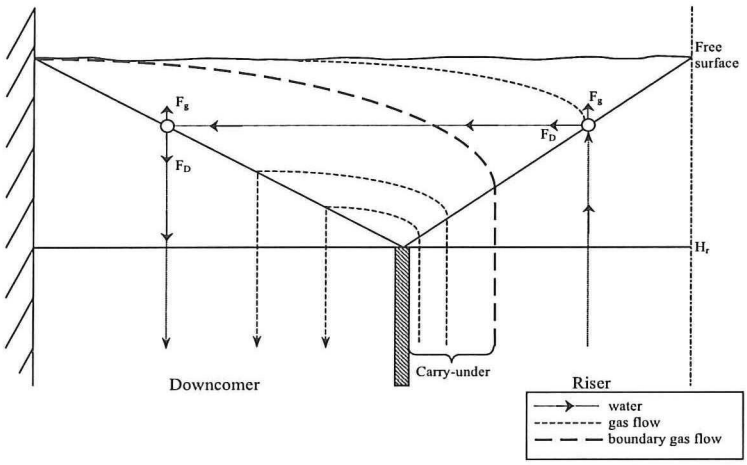

Figure E.1: Carry-under model of Lützow

The bold curve in figure E.1 is the boundary of the bubble flow, under this boundary all the gas bubbles move into the downcomer and above the boundary the gas bubbles leave the airlift through the free surface. The bubbles in the riser between the internal wall and this boundary cause the carry-under, because all the gas bubbles are dragged with the liquid into the downcomer. All the other bubbles escaped from the liquid flow.

The carry-under is dependent on different flow characteristics of the airlift loop reactor namely,

- Gas hold-up at the top of the downcomer
- Fraction of gas hold-up in the downcomer in comparison to the gas hold-up in the riser
- Depth (in z-direction) of the carry-under
- Liquid flow at the top of the downcomer
- Fraction of the liquid flow in the riser which will enters the downcomer
- Mass flow fraction of the gas in the downcomer
- Fraction volume flow of in the downcomer

Therefore, all these items are important to look at when analyzing the gas hold-up in the downcomer of the airlift loop reactor.

Bibliography

Akker, H. E. A. (2000). Fysische technologie van conversieprocessen en produktbewerkingen. *Coursebook Technische universiteit Delft, Faculteit Technische natuurwetensappen Scheikundige Technologie en Materiaalkunde.*

Auton, T. (1983). The dynamics of bubbles, drops and particles in motion in liquids. *Ph.D. thesis University of Cambridge.*

Couvert, A., Bastoul, D., Roustan, M., Line, A., and Chatellier, P. (2000). Prediction of liquid velocity and gas hold-up in rectangular airlift reactors of different scales. *Chemical Engineering and Processing, 40*, pages 113–119.

Elghobashi, S. and Abou-Arab, T. (1983). A two-equation turbulence model for two-phase flows. *Physics and Fluids, 26*, pages 931–938.

Ferziger, J. H. and Peric, M. (1999). Computational methods for fluid dynamics. *Springer.*

Fluent Inc. (1998). *Fluent 5 User's Guide.* Fluent Inc.

Lathouwers, D. (1999). Modelling and simulation of turbulent bubble flow. *Ph. D. thesis, Delft University of Technology, The Netherlands.*

Launder, B. E. and Spalding, D. B. (1974). The numerical computation of turbulent flows. *Computer Methods in Applied Mechanical Engineering, 3*, pages 269–289.

Loncle, C. (2000). 3d transient simulations of bubbly flow in a asymmetrically aerated flat bubble column. *Graduation Thesis, Delft University of Technology.*

Merk, H. (1980). Fysische stromingsleer. *course notes of Technische Hogeschool Delft, Laboratorium voor Aero- en Hydrodynamica, Nederland.*

Mudde, R. F. and Akker, H. E. A. (2001). 2-d and 3-d simulations of an internal airlift loop reactor on the basis of a two-fluid model. *Kramers laboratorium voor Fysische technologie, Delft University of technology.*

Mudde, R. F. and Simonin, O. (1999). Two and three dimensional simulations of bubble plume using a two fluid model. *Chemical Engineering Science*, pages 5061–5069.

Pan, Y. and Dudukovic, M. P. (2000). Numerical investigation of gas driven flow in 2-d bubble columns. *AiChE Journal, Vol 46*, pages 434–449.

Schwarz, M. and Turner, W. (1988). Applicability of the standard k-ϵ turbulence model to gas-stirred baths. *Applied Mathematic Modelling, 12*, pages 273–279.

Siegel, M. H. and Robinson, C. W. (1992). Applications of Airlift Gas-Liquid-Solid reactors in Biotechnology. *Chemical Engineering Science, Vol 47*, pages 3215–3229.

Simonin, O. (1990). Eulerian formulation for particle dispersion in trubulent two-phase flows. *Fifth workshop on two-phase flow predicionts, Erlangen, Germany*, pages 156–166.

Simonin, O. (1997). Prediction of the dispersed phase turbulence in particel-laden jets. *Gas-Solid Flows, 121*, pages 197–202.

Simonin, O. and Viollet, P. (1990). Precitcion of an oxygen droplet pulverization in a compressible subsonic coflowing hydrogen flow. *Numerical methods for Multiphase Flows, 91*, pages 73–82.

Sokolichin, A. (1994). Gas-liquid flow in bubble columns and loop reactors: Parti. detailed modelling and numerical simulation. *Chemical Engineering Science, Vol 49*, pages 5735–5746.

Sokolichin, A., Eigenberger, G., Lapin, A., and Lubert, A. (1997). Dynamic numerical simulations of gas-liquid two-phase flows. *Chemical Engineering Science, 52*, pages 611–626.

Thomas, N. H., Auton, T. R., Sene, K., and Hunt, J. C. R. (1983). Entrapment and transport of bubbles in transient large eddies in multiphase turbulent shear flows. *International Conference on the Physical Modelling of Multi-Phase Flows*, pages 169–184.